Principles and applications of sono-optogenetics

Fan Yang^{1,2,4}, Seong-Jong Kim^{3,4}, Xiang Wu^{1,2}, Han Cui^{1,2}, Sei Kwang Hahn³, and Guosong Hong^{1,2,*}

- ¹ Department of Materials Science and Engineering, Stanford University, Stanford, CA, 94305, USA
- ² Wu Tsai Neurosciences Institute, Stanford University, Stanford, CA, 94305, USA
- ³ Department of Materials Science and Engineering, Pohang University of Science and Technology (POSTECH), 77 Cheongam-ro, Nam-gu, Pohang, Gyeongbuk, 37673, Republic of Korea
- ⁴ These authors contributed equally to this work.
- * Corresponding author: guosongh@stanford.edu

Abstract

Optogenetics has revolutionized neuroscience research through its spatiotemporally precise activation of specific neurons by illuminating light on opsin-expressing neurons. A long-standing challenge of *in vivo* optogenetics arises from the limited penetration depth of visible light in the neural tissue due to scattering and absorption of photons. To address this challenge, sono-optogenetics has been developed to enable spatiotemporally precise light production in a three-dimensional volume of neural tissue by leveraging the deep tissue penetration and focusing ability of ultrasound as well as circulation-delivered mechanoluminescent nanotransducers. Here, we present a comprehensive review of the sono-optogenetics method from the physical principles of ultrasound and mechanoluminescence to its emerging applications for unique neuroscience studies. We also discuss a few promising directions in which sono-optogenetics can make a lasting transformative impact on neuroscience research from the perspectives of mechanoluminescent materials, ultrasound-tissue interaction, to the unique neuroscience opportunities of "scanning optogenetics".

1. Introduction

Neuromodulation enables the dissection of the causal relationship between neural activity and specific behaviors by stimulating targeted sites in the nervous system [1]. Since the introduction of cardiac pacemaker technology in the late 1960s, electrical neuromodulation in the brain [2,3], spinal cord [4], and peripheral nerve [5,6] has facilitated the diagnosis and treatment of neurological disorders and associated symptoms. However, it remains a fundamental challenge for stimulating electrodes to achieve cell-type specific neuromodulation [7–9]. Optical neuromodulation addresses this challenge by leveraging the advances in fiber optics and genetics [10,11]. As the most prominent method of optical neuromodulation, optogenetics enables spatiotemporally precise illumination in the neural tissue for targeted activation and inhibition of neuronal activity by activating opsins genetically expressed in specific neurons. Compared to most electrical neuromodulation methods, optogenetics offers neuron-type specific activation and inhibition in live animals, thus providing a toolbox of neural circuit-breakers for

dissecting the neural circuitry underlying specific behaviors and disorders [9]. A practical challenge of optogenetics and other optical neuromodulation methods [12-14] arises from the limited penetration depth of light due to the strong photon scattering in the visible range in the neural tissue [15,16]. Specifically, visible photons are strongly scattered and absorbed in the neural tissue, leading to >90% attenuation of incident photons through merely 1 mm brain tissue. To mitigate this challenge, emerging optogenetic technologies have been developed with red-shifted opsin activation spectra, improved opsin sensitivity, as well as novel light delivery strategies [17-22]. Among these emerging optogenetic technologies, sono-optogenetics represents an attractive alternative to conventional fiberbased optogenetic methods by replacing the brain-invasive, head-tethered optical fiber with tissue-penetrant focused ultrasound (FUS) [23,24]. Specifically, FUS activates the mechanoluminescence from blood-circulating mechanoluminescent nanotransducers (MLNTs) in the brain, thus realizing a minimally invasive method for delivering light to specific brain targets and activating opsin-expressing neurons therein. Due to the deeppenetrated depth of FUS (~centimeters) and the capability to quickly change its focus, sono-optogenetics offers unique opportunities for neuroscience studies and the clinical translation of optogenetics.

In this review, we present an overview of the sono-optogenetics method from the underlying physical principles to its neuroscience applications. We first discuss the background and some technical challenges of current optogenetics methods. Subsequently, we discuss the fundamentals of ultrasound, mechanoluminescent (ML) materials and their synthetic routes, trap states and their contribution to the ML process, as well as some strategies to optimize ML emission. Next, we review a handful of reported examples of applying sono-optogenetics in live animals. We conclude this article with a brief summary and point out potential challenges and strategies for adopting this emerging method for neuroscience studies.

2. Optogenetics

2.1 Background of optogenetics

The emergence of laser technology has motivated the development of optical neuromodulation methods since the 1970s [25]. Although these more conventional neuromodulation methods benefit from wireless energy delivery and high spatiotemporal resolution, they cannot differentiate among different neuron types, and the hypothesized mechanism of action is via the photothermal effect [26,27]. Light-sensitive materials, such as photovoltaic silicon membranes and molecules that can undergo photoisomerization, have also been leveraged for optical neuromodulation based on nonthermal effects [13,28]. Besides these non-genetic optical neuromodulation approaches, advances in genetics and molecular biology have led to the development of optogenetics for cell-type specific photostimulation of transgenic neurons [29]. Optogenetics represents a

transformative neuroscience method that enables temporally precise control of neural activity with light [30]. Specifically, incident light activates opsins, light-gated ion channels which are expressed in specific cell populations, yielding excitatory or inhibitory stimulation of targeted cells depending on the depolarizing or hyperpolarizing nature of the specific opsin [31]. The unique ability to dissect and manipulate neural circuitry by controlling the genetically targeted neuron subtypes and pathways of the nervous system has since motivated the development of various approaches for light delivery in the brain and peripheral nerve targets [32,33]. Importantly, optogenetics is widely applied in the deep brain, where the neural activity in deep-brain nuclei has been implicated in many neurological and neurodegenerative diseases [34]. The need to efficiently deliver light into these deep-brain nuclei without incurring significant damage to the brain tissue thus represents a major motivation behind sono-optogenetics and other advanced optogenetic methods.

2.2 Challenges of light delivery in optogenetics and emerging optogenetic methods

Light delivery in the brain represents a practical challenge for *in vivo* optogenetics. Visible light, which is used to excite most opsins in optogenetics, cannot penetrate into the deep brain region due to scattering in the tissue and absorption by the endogenous chromophores therein [15,35]. As a result, to deliver light efficiently into the deep brain, implanted optical fibers are usually used for *in vivo* optogenetics [32,36,37]. However, the fiber implantation process represents an invasive procedure, causing permanent brain damage along the path of implantation [38]. In addition, the mechanical mismatch between the rigid fiber material and soft brain tissue usually results in a chronic immune response at the fiber interface, necessarily disturbing the local neuronal and glial populations while degrading the long-term performance of the fiber interface [39]. Furthermore, the optical fiber tethered to the skull restrains the subject's naturalistic behavior, thus interfering with the free motion and social interactions of the animals under study [40].

Several emerging methods aim to overcome the challenges of *in vivo* light delivery for deep-brain optogenetics. Specifically, red-shifted opsins leverage wavelength-dependent scattering of photons in the brain, achieving optogenetic neuromodulation in the deeper tissue with red illumination (**Fig. 1a**) [17,35,41,42]. Additionally, ultra-sensitive opsins can be activated by transcranial illumination despite the strong attenuation of light intensity across the brain tissue (**Fig. 1b**) [18,43]. Besides these genetic engineering approaches, materials science has also facilitated deep-brain optogenetics and enabled alternative genetic neuromodulation approaches. For example, upconversion nanoparticles (UCNPs) that convert 980-nm near-infrared (NIR) light into local 470-nm blue emission have enabled transcranial optogenetics in freely behaving mices (**Fig. 1c**) [19,44,45]. Besides these conventional opsins, transient receptor potential (TRP) channels, which

are the molecular basis of infrared sensitivity in rattlesnakes [46], have also been employed in emerging optogenetic systems. For example, TRPV1 ion channels sensitized by semiconducting polymeric nanotransducers termed MINDS (macromolecular infrared nanotransducers for deep-brain stimulation) have been shown to respond to brain-penetrant, 1064-nm infrared light (Fig. 1d). This "infrared optogenetics" approach enables remote neuromodulation of behaving mice with widefield, overhead illumination that can penetrate through the intact scalp, skull, and at least 5 mm of the brain tissue [47].

Despite these advances in emerging optogenetic methods, several challenges remain. First, none of these methods can achieve deep-brain optogenetics without removing the intact scalp of the subject. Since the removal of the scalp usually results in a significant drop in cortical temperature and the ensuing alteration of neural activity, it is desirable to keep an intact scalp for in vivo optogenetic modulation of the brain[48]. Second, many of the materials-enabled methods still require intracranial injection of optical materials (e.g., UCNPs and MINDS), thus causing damage to the endogenous neural tissue. Third, despite the demonstrated transcranial brain penetration of long-wavelength illumination, none of the existing approaches enables easy relocation of a spatially confined illumination spot in the three-dimensional (3D) brain tissue. This limitation results from the diffuse nature of light (i.e., cortex-impinging light cannot be focused in the deep brain) and the invasive nature of fiber implants (i.e., an implanted fiber cannot be easily relocated without incurring additional damage) in brain tissue. Consequently, existing optogenetic approaches usually result in limited throughput in terms of the number of disparate brain regions that can be simultaneously or sequentially manipulated in the same subject.

3. Ultrasound and its interaction with matter

Ultrasound is commonly generated by piezoelectric transducers, which convert electrical charges into mechanical vibration waves. The resulting mechanical wave can propagate over a substantial distance in a fluid or solid, depending on the frequency of the wave. Owing to its deep penetration in biological tissue, ultrasound has been broadly used as a non-invasive technology for clinical imaging. Based on its frequency, conventional ultrasound can be classified into three categories: low (<1 MHz), medium (1–5 MHz), and high (5–10 MHz) frequency ultrasound [49]. Low frequency ultrasound benefits from deep penetration in living tissues at the cost of low spatial resolution, while high frequency ultrasound exhibits shallow tissue penetration and high spatial resolution. To focus ultrasound into a diffraction-limited spot, a curved transducer or a phased array is usually employed to obtain a high power density at the focus and achieve sufficient spatial resolution for imaging as well as targeted tissue modulation and ablation. Specifically, upon interactions with living biological tissues, focused ultrasound (FUS) can generate a

combination of mechanical, thermal, and chemical effects [50]. In addition, FUS can also interact with ML materials to produce light emission. We discuss each of these processes discussed in the following sections.

3.1 Interactions of FUS with biological tissues

When FUS is applied to a fluid, acoustic cavitation is generated when the local pressure of the fluid drops below its saturated vapor pressure. The minimum negative pressure required to form a cavity (i.e., a gas bubble) is the cavitation threshold. After the bubbles are formed, they expand during the rarefaction phase of the FUS and shrink during the compression phase. As a result, the bubbles oscillate in response to the ultrasound. Based on the energy of FUS and the competition between the gas pressure and liquid inertia, cavitations can be classified into two types: inertial and non-inertial [51]. In non-inertial cavitation, the bubble undergoes sustained oscillations without collapsing, and the oscillatory motion of the bubble is dominated by the pressure factor. In inertial cavitation, the bubble undergoes rapid collapse due to the dominance of the liquid inertia. The collapsed bubble may then regrow into a new bubble with a radius at least twice the initial size, or it may disintegrate.

When a bubble oscillates and collapses in the biological tissues, it can generate an array of secondary mechanical effects (Fig. 2). i) Microstreaming occurs when oscillating bubbles transfer their momentum to the surrounding liquid, causing the latter to flow [52]. Microstreaming can produce shear stress on the adjacent biological tissue, potentially promoting drug release from carriers and enhancing tissue permeability. ii) Microjets are produced when a bubble collapses near a surface [51]. The microjet can travel with supersonic velocity toward the surface, causing pitting even in hard surfaces such as that of steel. The same mechanical impact of the microjet, within the safety range of not causing tissue damage, can be leveraged to facilitate tissue permeabilization and drug release [53]. iii) Shockwaves are produced during the collapse of an inertial bubble, which results in a discontinuity in the pressure of the surrounding fluid. The emission of a shockwave imposes a large stress on the nearby surface; therefore, it has been leveraged for drug release by disrupting micelles and liposomes [54,55].

Besides these secondary mechanical effects, FUS also produces thermal effects via the nonlinear acoustic radiation force and viscous friction of oscillating bubbles inside the tissue. The thermal effect can also be leveraged in therapeutics such as thermal ablation of target tissues as well as drug release facilitated by temperature-sensitive carriers [56]. Lastly, during the violent implosion of bubbles, the temperature increase inside the collapsing cavitation can well exceed the typical thermal effect outside the bubble. Specifically, a rapid bubble compression can lead to an extreme temperature reaching several thousand Kelvins for a very brief period of time (usually <1 µs) [50]. The collapsing bubbles are usually also associated with the emission of light, also known as sonoluminescence. In addition, collapsing bubbles also create reactive oxygen species

(ROS), due to the pyrolysis of water. This chemical effect of FUS can be employed for cancer therapy, acceleration of chemical reactions (sonochemistry), and even mechanoluminescence from organic luminescent molecules [57].

3.2. Interactions of FUS with ML materials

Besides the interaction between FUS and biological tissues, FUS also produces mechanical stress upon impinging on solid-state materials. ML materials represent a group of solid-state materials that produce light emission in response to a mechanical stress, thus offering new opportunities for FUS-mediated light emission. Here we review the history, mechanism, and materials of mechanoluminescence, with a focus on trapcontrolled ML materials.

3.2.1. Mechanoluminescence

Dating back to 1650, Francis Bacon discovered light emission by scratching or crushing hard sugar with a knife. This discovery represents the first report of the ML phenomenon [58]. Since then, a number of ML phenomena have been observed by crushing certain mineral crystals and chemical compounds [59,60]. In early samples, ML emission was attributed to fractoluminescence since these processes were associated with the fracture and destruction of solids. As an irreversible process, fractoluminescence yields weak and non-repeatable light emission with limited practical applications. Furthermore, the lack of proper characterization methods prevents researchers from fully leveraging the ML process for practical applications. In 1999, Xu et al. reported ML materials with robust and reproducible green (SrAl₂O₄:Eu²⁺) [61] and yellow (ZnS:Mn²⁺) [62] emission under mechanical stress. These discoveries marked a key milestone in the modern research of ML. This bright ML can be self-recovered after being charged with UV light and released with cyclic mechanical loading. These unique properties have since attracted broad interest in ML research, thus enabling multiple applications from the detection of structural cracks [63,64], stress sensing in wearable devices [65], monitoring the biomechanics of bones and teeth [66,67], to sono-optogenetics for minimally invasive neuromodulation [23,68].

ML is usually classified into three categories: fractoluminescence, triboluminescence, and elasticoluminescence (**Fig. 3**). Fractoluminescence is generated from the separation and recombination of opposite charges when ionic and covalent bonds are broken in solid materials (**Fig. 3a**). Most inorganic and organic crystals emit light upon fracturing, although the irreversible physical damages to the material usually result in one-off ML emission, thus limiting their utility as a long-term light source. In addition, triboluminescence originates from the direct contact between two materials (**Fig. 3b**). It has been hypothesized that contact electrification as a result of mechanical deformation contributes to triboluminescence. Specifically, it has been found that the triboelectric

potential can reach 400 V locally, high enough to induce electroluminescence from crystalline ZuS:Cu⁺ [69]. Lastly, elasticoluminescence involves the elastic deformation of the host material, which generates ML signals under repeated mechanical stimuli without fracture or damage to the material (**Fig. 3c**). Specifically, the intensity of elasticoluminescence usually increases linearly with the applied mechanical stress. A prevalent model of elasticoluminescence attributes its origin to the coupling of strain-induced piezoelectricity and electroluminescence under the piezoelectric field.

As a caveat to the above categorization of ML, oftentimes these three mechanisms are closely related to one another with more than one of them involved in the ML of the same material. For example, an ML material may present elasticoluminescence when the mechanical load is within the range of the elastic deformation, while the same material may show fractoluminescence beyond the fracture point. Furthermore, some ML materials (e.g., ZnS:Mn) generate sufficient piezoelectricity under both compressive and shear stress, thus leading to both elasticoluminescence and triboluminescence, respectively, in the same material.

Although the exact mechanism of ML emission for a specific material may be obscure, trap-controlled ML materials provide a model system for understanding the ML process in these materials under mechanical stress. A characteristic feature of trap-controlled ML materials is that they can reproducibly generate ML emission in response to cyclic mechanical stimuli without damaging the material. The reproducible emission in trap-controlled ML materials is usually achieved in two steps: i) trapping of charge carriers (i.e., electrons or holes) in the trap states; and ii) de-trapping of charge carriers under mechanical stimulus, yielding light emission. Below we discuss the origin of trap states, strategies to synthesize trap-controlled ML materials, and the mechanism behind trap-controlled ML emission.

3.2.2 Trap states in mechanoluminescent materials

Trap-controlled ML materials are usually composed of inorganic host materials doped with transition-metal and rare-earth ions. In these materials, the trap state can be formed via the following two processes. i) The trap state does not exist in the original host materials and is formed by high-energy irradiation, such as X-ray or γ-ray irradiation. In this case, the trap states strongly depend on the composition of the host materials and the dose of high-energy radiation. Specifically, these ML materials include X-ray or γ-ray irradiated alkali/alkaline earth halide and ZnS crystals [70–72]. ii) The trap state is generated during the preparation of the host material and does not involve high-energy irradiation. In these materials, the concentration and trap depth can be tuned by specific dopants made of rare-earth and transition-metal elements, the stoichiometry of precursors, and the synthetic method. Since the first report of SrAl₂O₄:Eu²⁺ and ZnS:Mn²⁺ ML materials more than two decades ago, this type of trap-controlled ML materials has

attracted broad research interest in ML materials research. Several bright trap-controlled ML materials are $Sr_2MgSi_2O_7$:Eu,Dy, $CaAl_2Si_2O_8$:Eu²⁺, $ZnS:Cu^+/Mn^{2+},Te^{2+}$, $CaZnOS:Tb^{3+}/Eu^{3+}/Sm^{3+}/Yb^{3+}/Er^{3+}/Pr^{3+}/Tm^{3+}/Dy^{3+}/Ho^{3+}/Sm^{3+}/Nd^{3+}$, (Ba,Ca)TiO₃:Pr³⁺, NaNbO₃:Pr³⁺, etc.. We focus on the second type of trap-controlled ML materials in this review.

From the perspective of materials science, carrier traps in trap-controlled ML materials are normally regarded as point defects in host materials. These point defects can be created by doping or nonstoichiometry of the precursors during synthesis. Specifically, the doping strategy includes non-equivalent substitution and equivalent substitution. On one hand, non-equivalent substitution refers to the substitution of monovalent or divalent metal cations (M⁺/M²⁺) in the host by trivalent rare-earth dopants (Ln³⁺). For example, when three divalent metal cations (M²⁺) are substituted by two trivalent rare-earth dopants (Ln³⁺), two types of defects are generated simultaneously, according to the equation below:

$$Ln_2O_3 + 3M_M^{\times} \rightarrow 2Ln_M^{\cdot} + V_M^{"} + 3MO$$

where the negatively charged vacancy $V_M^{"}$ and the positively charged substitutional atom $Ln_M^{"}$ act as hole and electron traps, respectively. On the other hand, equivalent substitution occurs in alkaline-earth metal (M^{2+} = Ca^{2+} , Sr^{2+} , Ba^{2+})-based ML materials. For example, Eu^{2+} and Mn^{2+} ions can replace M^{2+} in these materials. Although the net charge is neutral for these substitutional atoms, the electronegativity of Eu^{2+} and Mn^{2+} ions is different from alkaline-earth cations, thereby leading to isoelectronic traps [73]. Besides the doping strategy, the nonstoichiometry approach leverages a non-integer elemental ratio in the host material; that is, the number of cations or anions is slightly more or less than that in a stoichiometrically perfect lattice. In this case, point defects, such as oxygen/sulfide vacancies or cation vacancies are introduced, acting as electron or hole traps, respectively.

3.2.3 Synthesis of trap-controlled ML materials

Trap-controlled ML materials are conventionally synthesized via solid-state reactions, the sol-gel method, and the ultrasonic spray pyrolysis technique. To fulfill the trap engineering requirement as discussed in 3.2.2, introducing point defects to host materials of the desired phase necessitates high-temperature treatment. Therefore, all conventional methods require reaction or annealing at an elevated temperature, necessarily yielding large, micrometer-sized particles incompatible with minimally-invasive syringe-assisted *in vivo* delivery. To address this challenge, recently our lab reported a novel biomineral-inspired approach for preparing trap-controlled ML colloids. In the following sections, we

provide a comprehensive overview of the three conventional methods along with our new approach for synthesizing trap-controlled ML materials.

Solid-state reactions

Solid-state reactions represent the most straightforward and efficient method for preparing crystalline ML materials. Historically, most of trap-controlled ML materials were first reported with their synthesis via this method. In a typical solid-state reaction, the precursors are thoroughly ground using a mortar and pestle, followed by reactions at elevated temperatures (typically > 1000 °C) for several hours. An additional grinding process is usually involved after the products are cooled to room temperature. Solid-state reactions usually benefit from their simplicity, large-scale production, as well as bright ML emission of the product. However, the reaction at high temperatures for hours necessarily results in large-grained (>10 µm) products. The products of solid-state reactions are usually less favorable for biomedical applications since the micron-sized particles prohibit their in vivo delivery via the common systemic administration route. Specifically, large particles impose the risk of blocking the microvasculature, especially capillaries, after systemic administration. Moreover, large particles may trigger macrophagic uptake and rapid blood clearance mediated by the mononuclear phagocyte system (MPS). Albeit unfavorable, high-temperature treatment is usually required for creating sufficient point defects, which act as trap states to store photon energy, in host materials of desirable polymorphs. It is not surprising to note that the two following methods involve a similar high-temperature annealing step for preparing trap-controlled ML materials as well.

The sol-gel method

The sol-gel method acts as a mild chemical route to synthesizing MLNTs. A typical solgel method involves two steps: i) the formation of metal-chelates from an aqueous solution of metal precursors and ii) the polymerization of metal-chelates to form clusters of the product. Specifically, metal salts dissolved in an aqueous solution are usually mixed with chelating agents, such as citric acid, ascorbic acid, ethylene diamine tetraacetic acid (EDTA) to form metal-chelates. In some cases, a crosslinking agent, such as a polyhydroxy alcohol (e.g., ethylene glycol, EG, or polyethylene glycol, PEG), is added to the previous mixture to produce polymeric resin gels on a molecular level. The crosslinking agent is believed to facilitate compositional homogeneity and size uniformity of resulting particles [74]. A salient advantage of the sol-gel method lies in the ability to tune the particle size and morphology via changing the molecular weight of PEG and the ratio of the chelating agent to PEG. After the chelation and gelation step, the intermediate is still subject to post-annealing at an elevated temperature (500~1000 °C) to obtain the desired phase of the host material and improve uniform doping of trap states. Importantly, the post-annealing process burns off all organic additives on the surface of nanocrystals, resulting in aggregated, large particles with broad size distributions from nanometers to micrometers.

The ultrasonic spray pyrolysis technique

The ultrasonic spray pyrolysis technique is a straightforward aerosol synthetic method to prepare nanoparticles. To implement this technique, the synthetic system is composed of an ultrasonic atomizer that generates aqueous droplets containing the precursors and a furnace for high temperature calcination of the droplets [75]. This method usually yields spherical particles as a result of the spherical aerosol droplets. Further, the particle size distribution is mainly determined by the diameter of the droplet, which is in turn related to the frequency of the ultrasonic atomizer and the precursor concentration [76]. As an example, the ultrasonic spray pyrolysis technique has been used to prepare spherical SrAl₂O₄:Eu²⁺ nanoparticles with sizes in the range of 10-30 nm [77]. A remaining challenge of this approach arises from the inevitable aggregation of nanoparticles due to the coalescence of the aerosol droplets during calcination.

The biomineral-inspired approach

As discussed above, the elevated temperature leads to large ML particles and aggregates during solid-state reactions, post-annealing in the sol-gel method, and calcination in the ultrasonic spray pyrolysis technique. An intuitive strategy to avoid aggregation or coalescence of MLNTs is thus making ML colloids after any high-temperature treatment in a top-down approach. To this end, our group recently developed a biomineral-inspired approach by leveraging the demineralization found in nature (Fig. 4) [68,78]. Demineralization of natural biominerals (e.g., seashells, bones, and dental enamel) exhibits a self-preservation behavior, in which the biominerals can gradually dissolve to nanoparticles in an undersaturated microenvironment. Remarkably, the resulting nanoparticles are resistant to further dissolution despite their thermodynamic metastable nature. We applied the biomineralization approach to produce colloidal ML nanocrystals from a wide range of bulk silicate, aluminate, and sulfide phosphors from solid-state reactions (Fig. 4a). The as-prepared ML colloids are as small as 20 nm while preserving the strong ML emission of their bulk counterparts in the spectral range of 470~610 nm (Fig. 4b and c). Therefore, the biomineral-inspired approach represents a unique method for synthesizing stable and bright ML colloids for biomedical applications that we discuss in greater detail below.

3.2.4 Mechanisms of trap-controlled mechanoluminescence

In this section, we summarize typical models to explain trap-controlled ML. Specifically, we explain capture of charge carriers by trap states, piezoelectricity-induced de-trapping process under mechanical stimulus and associated luminescence emission in detail.

Carrier trapping and release

There are two proposed carrier traps (hole traps and electron traps) in the ML process (**Fig. 5**). Taking $SrAl_2O_4$: Eu^{2+} as an example [61], in the first hole traps model, Eu^{2+} generates Eu^+ and a hole upon optical excitation (**Fig. 5a**). The hole escapes to the valence band and then can be captured by negative-charged Sr vacancies ($V_{Sr}^{"}$) that serve as hole traps. Under mechanical stimulation, the hole is released from the traps and recombined with Eu^+ to form excited Eu^{2+} . Then Eu^{2+} ions return to the ground state and emit green light. In the second model, oxygen vacancies serve as electron traps and electrons are regarded as carriers (**Fig. 5b**) [79]. Upon UV light excitation, Eu^{2+} ion in the ground state is excited to the conduction band and oxidized to a trivalent state Eu^{3+} accomplished with the generation of an electron simultaneously. This electron is trapped by oxygen vacancies ($V_O^{"}$). After applying mechanical stimuli, the electron is released from the trap and recombines with Eu^{3+} moving through the conduction band to form Eu^{2+} , finally emitting green light. It should be mentioned that in these two examples, the detail of the carrier de-trapping process under mechanical stress is not discussed. We refer the readers to the following section for the detailed discussion of the detrapping process.

Piezoelectricity-induced carrier de-trapping

As we mentioned in 3.2.1, piezoelectric property is required for ML emission. The mechanical stress-induced piezoelectric effect is believed to de-trap carriers during the ML emission. Because the lack of central symmetry is a prerequisite for piezoelectric materials, non-centrosymmetric crystal structure is usually required for materials to produce ML emission. Xu et al. has confirmed that among Eu²⁺-doped strontium aluminates (SrAl₁₂O₁₉, Sr₃Al₂O₆, SrAl₄O₇, Sr₄Al₁₄O₂₅, α-SrAl₂O₄, β-SrAl₂O₄, and their mixed phases), α-SrAl₂O₄ is the only polymorph without centrosymmetry, thus exhibiting ML emission [80]. In the piezoelectricity-induced electroluminescence model, the applied mechanical stress produces a strong piezoelectric field which is sufficient to directly induce electroluminescence. Specifically, this piezoelectric field results in the de-trapping and acceleration of electrons to the luminescent center to emit light. Several previous works have experimentally confirmed the presence of a strong piezoelectric field above the electroluminescence threshold [69,81]. However, the piezoelectricity-induced electroluminescence model can only explain the mechanoluminescence semiconducting (e.g. ZnS, (Ba,Ca)TiO₃) host materials that have reported electroluminescence properties. Moreover, this model cannot explain the ML emission under low mechanical stress that only produces a weak piezoelectric field well below the electroluminescence threshold.

To explain ML induced by a weak piezoelectric field, a piezoelectricity-induced carrier detrapping model is proposed (**Fig. 6**). In this model, ML materials excited by light generate charge carriers which are captured by trap states in the host matrix (**Fig. 6a**). Then mechanical stress is applied to the host matrix to locally produce a low piezoelectric field. Owing to a continuous distribution of trap states in their energy, the carriers captured in

shallow traps may be de-trapped to the conduction band under this weak, local piezoelectric field, before they subsequently return to the ground state accompanied with light emission (**Fig. 6b**). In contrast, de-trapping of carriers from the deep traps requires a stronger piezoelectric field and is thus usually not considered in this model.

3.2.5 Optimization of ML emission

Although an array of trap-controlled ML materials have been developed, ML emission from most materials is weak and invisible to the naked eye under ambient light. The weak ML emission thus makes these materials less ideal for specific biomedical applications where sufficient power density of illumination is required under minimum mechanical perturbation induced by FUS. To address this challenge, much of the recent effort has been contributed to improve the ML intensity of trapped-controlled materials.

The first strategy relies on modifying the microstructure of ML materials, informed by the full understanding of the structure-property relationship. Specifically, to optimize mechanoluminescence through activator dopants, a common method relies on co-doping the activator with transition-metal or rare-earth ions because the presence of co-dopants helps increase the number of trap states in the host matrix. The most prominent strategy leverages the combination of Eu²⁺ (activators) and Dy³⁺(co-dopants). For instance, Xu et al. reported that ML emission intensity increases around two orders of magnitude via codoping of Eu²⁺ and Dy³⁺ in Ca₂MgSi₂O₇ in comparison to Eu²⁺ singly-doped Ca₂MgSi₂O₇ [82]. They attributed the ML enhancement to the creation of shallow traps that were confirmed by the new emission band at low temperature range in the thermoluminescence spectrum. Besides optimizing the dopants, another strategy is based on screening the much larger family of persistent luminescent phosphors for polymorphs of the host material without centrosymmetry. A prominent fact attesting to this method is that most trap-controlled ML materials reported thus far possess both mechanoluminescence and persistent luminescence. As a strategy to optimize mechanoluminscence, substitution of ions in the host lattice may significantly enhance the emission since substitutional ions change the volume of the unit cells, thus increasing the piezoelectric coefficient by altering crystal symmetry. This ion substitution strategy has been employed in alkaline earth metal-based ML materials, such as (CaxSr₁- $_{x}$)Al₂Si₂O₈:Eu²⁺ [83], (Ca,Ba)TiO₃:Pr³⁺ [81], (Sr,M)₂MgSi₂O₇:Eu²⁺ (M = Ca, Sr, Ba) [84].

The second strategy for enhancing ML emission leverages an inorganic-organic composite architecture to enhance ML emission. To this end, researchers have designed specific array architectures to concentrate applied mechanical stress on specific spots in the polymeric matrix to obtain high mechanoluminescence. For example, Wang et al. fabricated a matrix composed of square array architecture with ZnS:Mn²⁺/photoresist pixels [85]. The array architecture design could well eliminate the crosstalk from adjacent pixels, resulting in a good resolution under weak stress. Later, Wang et al. upgraded the

square array to a pyramidal array [86]. The concentrated stress on the center of the pyramid achieved a pressure sensitivity threshold down to 0.6 kPa. Zhu et al. also reported micro-sized ZnS:Cu pillars PDMS arrays, the ML intensity in which is twice that prepared with a plain PDMS surface[87].

4. Sono-optogenetics

Sono-optogenetics is motivated by the challenges of *in vivo* light delivery for conventional optogenetics, the deep penetration and focusing ability of ultrasound in biological tissues, as well as light emission of trap-controlled ML materials under FUS-induced mechanical stress. Our group for the first time demonstrated that a circulation-delivered and rechargeable internal light source, which is mediated by tissue-penetrant FUS, can replace conventional fiber-based light illumination for minimally invasive optogenetic neuromodulation (Fig. 7a). Specifically, we synthesized ZnS:Aq,Co@ZnS core/shell MLNTs via a two-step hydrothermal process (Fig. 7b). The ZnS:Aq,Co@ZnS MLNTs exhibited mechanoluminescence centered at 470 nm under FUS stimulation with the ML spectrum highly overlapping with the activation spectrum of channelrhodopsin-2 (ChR2) (Fig. 7c). To demonstrate the feasibility of FUS-mediated sono-optogenetics, we systemically injected ZnS:Ag,Co@ZnS MLNTs into the blood circulation of mice, recharged these MLNTs during their circulation by 400 nm light in the superficial vessels, and discharged them with through-scalp FUS in the mouse brain to stimulate ChR2expressing neurons (Fig. 7d). Importantly, our in vivo experiments demonstrated the specificity of contralateral limb activation only in mice expressing ChR2 in the brain and injected with MLNTs (Fig. 7e and f). The lack of stimulated limb motion with ultrasound alone in the absence of ChR2 or MLNTs rules out the possibility of nonspecific neural activation with FUS. The biocompatibility of intravenously injected ZnS:Ag,Co@ZnS MLNTs was confirmed with a lack of any noticeable tissue damage or pathological lesion in the organs. This work represents the first proof-of-concept demonstration of minimally invasive sono-optogenetic neuromodulation with tissue-penetrant FUS and circulating MLNTs.

Besides our demonstration above, Chang et al. developed a magneto-luminescence microdevice (MLMD) to realize non-contact ML emission for optogenetic modulation (**Fig. 8**) [88]. The MLMD was constructed by integrating CaZnOS:Tb³⁺ ML phosphors into a container with a free-moving magnet bar, in which the magnet bar was controlled in a rotational motion by an external magnetic field to activate the ML phosphors to emit light. To study wireless neuromodulation with the MLMD in mice, the authors implanted the microdevice into the primary motor cortex of mice expressing the C1V1 opsin (**Fig. 8a**). Electrophysiological recordings exhibited a significant difference in the frequency and number of action potentials between mice with vs without the MLMD. Moreover, immunohistochemistry also revealed a higher expression level of c-fos, an immediately

early gene that labels recent neuron activity, in the brain of mice with MLMD stimulation than in all control groups (**Fig. 8b**). Furthermore, behavioral tests revealed a significant difference of locomotion in C1V1 mice with MLMD, indicating effective optogenetics by ML stimulation (**Fig. 8c**). In addition to neuromodulation, the authors utilized the MLMD to stimulate a photosensitive protein KillerRed, which generates ROS in response to 544 nm light emitted by the MLMD for subcutaneous antitumor therapy. During the treatment with implanted MLMD under the magnetic field, a negligible change in the mouse body weight was found along with minimal tissue damages in H&E stained organ slices, suggesting the good compatibility of MLMD. Although this work provided an innovative approach to deliver ML light for neuromodulation, the invasiveness may still be a concern for bioapplications.

Recently, our group developed a biomineral-inspired approach to prepare ML colloids with a broad range of compositions and emission wavelengths (Fig. 9) [68]. This method enables us to synthesize Sr₂MgSi₂O₇:Eu,Dy, ZnS:Cu,Al, ZnS:Mn, and CaTiO₃:Pr colloidals in a stable aqueous suspension with ML emission at 470 nm, 534 nm, 578 nm, and 610 nm, respectively, under hydrodynamic FUS stimulation. Importantly, this approach produces water-soluble ML colloids with sizes down to 20 nm, not only avoiding the blockage of blood capillaries after systemic delivery, but also fitting into the suitable size range (10-200 nm) of nanoparticles for long circulation time in vivo [89], which is desirable for in vivo biomedical applications. Since this approach well preserves the crystallinity of the solid-state precursor particles, the resulting colloids exhibit intense mechanoluminescence. Importantly, the ML of the Sr₂MgSi₂O₇:Eu,Dy colloids was much stronger than that of previously-reported ZnS:Ag, Co@ZnS MLNTs from a two-step hydrothermal route. We characterized the rechargeable emission of all ML colloidal nanocrystals in an artificial circulation tubing, observing reproducible emission at each corresponding wavelength with consistent intensity under repeated FUS pulses (Fig. 9a). In addition, we measured fast onset and offset kinetics of ML emission when FUS is applied and removed to the colloids, obtaining a short onset time of ≤5 ms for all materials regardless of the FUS duration (Fig. 9b). The fast temporal kinetics and diverse wavelengths of mechanoluminescence thus facilitate the application of these materials for sono-optogenetic activation of both excitatory (e.g., ChR2) and inhibitory opsins (e.g., eNpHR). Leveraging the rich vasculature throughout the entire mouse body, we systemically delivered Sr₂MgSi₂O₇:Eu,Dy colloids and applied FUS to the liver, kidney, and brain of the mouse (Fig. 9c). Reproducible blue light emission corresponding to the focal point of ultrasound can be observed from all tested organs, revealing a high spatial resolution of 150-500 µm approaching that of typical optical fibers (Fig. 9d). To evaluate the biosafety of Sr₂MgSi₂O₇:Eu,Dy colloids, we carried out biodistribution, excretion, and

histological analyses in mice after systemic delivery of these colloids, identifying negligible adverse effects [78]. Lastly, we confirmed the efficacy of sono-optogenetics in Thy1-ChR2-YFP transgenic mice expressing ChR2 (**Fig. 9e**). Applying immunostaining of c-fos, we found an obvious increase in expression level of c-fos in the Thy1-ChR2-YFP mouse brain compared to that in wild-type C57BL/6J mice (**Fig. 9f&g**). This result also rules out the possibility of nonspecific, direct neural activation with FUS in the mouse brain since the wild-type mouse brain exhibits minimal baseline activity even in the presence of FUS.

5. Conclusion and outlook

In this review, we present a comprehensive overview of the principles and applications of sono-optogenetics. The sono-optogenetic approach is motivated by the limited tissue penetration of visible light in *in vivo* optogenetic applications and enabled by the focusing ability of tissue-penetrant ultrasound as well as circulation-delivered MLNTs. In addition, the interactions between FUS and biological tissues as well as the underlying mechanism of FUS-stimulated emission in trap-engineered ML materials set the physical constraints for the application of this approach. Here, we summarize the challenges, methods for improvement, and potential directions from the perspectives of materials, ultrasound, and neuroscience for future sono-optogenetics research:

1) ML materials: despite the development of various trap-controlled ML materials, the mechanoluminescence of most materials remains weak and below the intensity requirement for specific biological applications such as optogenetics. Developing new piezoelectric host materials with strong emission based on current materials is highly desirable; The ML intensity of piezoelectric polymer composites has demonstrated ML enhancement [90]; therefore, piezoelectric polymer coating on ML particles can potentially increase the ML emission intensity. Besides improving the emission intensity, for the future sono-optogenetics research, replacing the current UV-based charging scheme with self-charged triboluminescence represents another promising direction. Lastly, the use of organic ML materials and mechanophores may offer new opportunities toward the clinical translation of sono-optogenetics owing to their improved biocompatibility [57,91,92]. Previous works have reported the generation of ROS from specific organic sonosensitizers with sonodynamic properties under FUS stimulation [93,94]. The generation of ROS is a double-edged sword. On one hand, the produced ROS under FUS can generate chemiluminescence in the presence of chemiluminescent molecules, thus yielding ultrasound-triggered in situ photon emission for optogenetics [57,95]. On the other hand, excessive ROS may cause damage to the brain by inducing apoptosis and disrupting the blood-brain barrier [96,97]. To avoid undesirable biological effects induced by ROS, it is important to use organic ML materials with their ROS

generation under control and spatially confined to only react with chemiluminescent molecules for sono-optogenetics.

- 2) Focused ultrasound: FUS is known to produce nonspecific neuromodulation, likely resulting from a combination of neuron membrane capacitance change [98], activation of mechanosensitive ion channels [99], and even activation through auditory pathways [100–102]. Specifically, it has been found that direct ultrasound neuromodulation in the mouse brain has a frequency dependence, with an increasing threshold in FUS intensity to achieve the same effect as the center frequency increases [103]. In addition, the pulse repetition frequency (PRF) of FUS has also been found to evoke the response of excitatory and inhibitory neurons differently [104]. In contrast, many of the ML colloids synthesized in our lab do not show enhanced sensitivity toward a specific frequency or PRF of FUS. This difference in neuron vs ML material response to FUS thus enables researchers to design specific FUS protocols to achieve sono-optogenetic activation of specific neuron populations by leveraging light emission from ML materials while minimizing direct FUS neuromodulation. Importantly, our preliminary results have demonstrated specific behavioral and immunohistochemical activation with sonooptogenetics, thus ruling out the possibility of nonspecific, direct neural activation with FUS in the mouse brain [23,68].
- 3) Neuroscience studies: as discussed in 2.2 above, deep-tissue light delivery represents one of the major challenges for in vivo optogenetics. Furthermore, the inability to reposition the illuminated region in the same animal's brain represents another challenge with conventional implants (e.g., fibers and light-emitting diodes) for optogenetics. In contrast, intravenously delivered MLNTs circulate in the bloodstream and emit light at any location or depth in the mouse brain determined by the focus of impinging ultrasound. This "virtual" light source can thus produce on-demand and dynamically programmable light emission patterns throughout the entire brain of live mice with millisecond precision, enabling unique opportunities for "scanning optogenetics". The "scanning optogenetics" approach, which represents a unique advantage of sono-optogenetics, can enable neuroscientists to rapidly turn on and off multiple brain regions simultaneously or sequentially in the same subject with a high throughput. As a proof-of-concept example, our recent work demonstrates a flexible and wireless multicolor display composed of different combinations of MLNTs and perovskite quantum dots in a silicone elastomer with each pixel individually addressed by scanning FUS to produce localized emission [105]. This scanning approach may allow for the dissection of the unique and/or synergistic contributions of different brain regions to a certain behavior or pathology of interest, such as the drug seeking behavior, in the same subject and experiment.

Acknowledgment

G.H. acknowledges three awards by NIH (R01NS126076-01, 1R34NS127103-01, and 5R00AG056636-04), a National Science Foundation (NSF) CAREER Award (2045120),

an NSF EAGER Award (2217582), a Rita Allen Foundation Scholars Award, a Beckman Technology Development Grant, a grant from the focused ultrasound (FUS) Foundation, a gift from the Spinal Muscular Atrophy (SMA) Foundation, a gift from the Pinetops Foundation, two seed grants from the Wu Tsai Neurosciences Institute, and two seed grants from the Bio-X Initiative of Stanford University. X.W. acknowledges the support by a Stanford Graduate Fellowship.

Figures

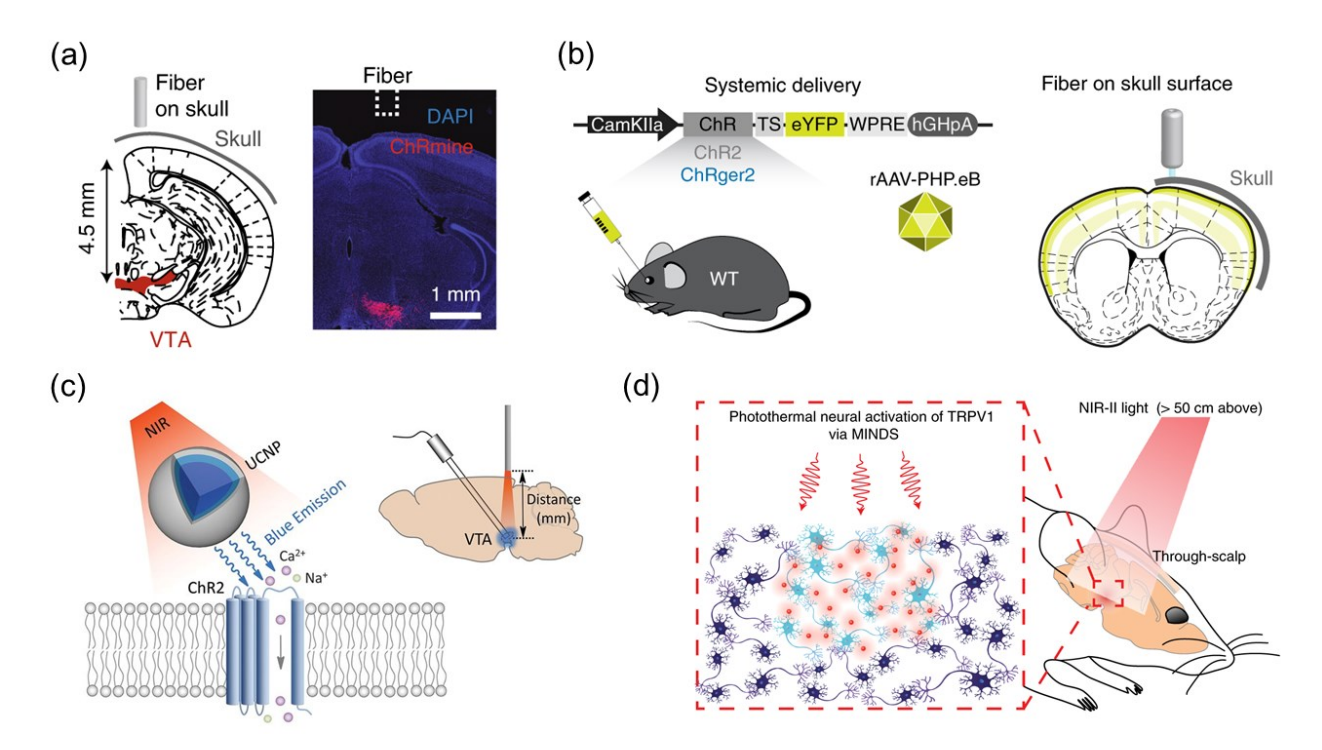


Fig. 1. Emerging optical neuromodulation methods. (a) A red-shifted and ultrasensitive opsin, ChRmine, enables transcranial deep-brain optogenetics with 635 nm illumination. Reproduced from [17] with permission from Springer Nature, Copyright 2021. (b) A high-photocurrent and low-light-sensitive opsin, ChRger2, enables transcranial optogenetics with 447 nm illumination. Reproduced from [18] with permission from Springer Nature, Copyright 2019. (c) UCNPs composed of NaYF4:Yb,Tm@NaYF4 enables transcranial activation of ChR2 under 980-nm illumination. Reproduced from [19] with permission from American Association for the Advancement of Science, Copyright 2018. (d) Polymeric nanoparticles enable through-scalp and tether-free neuromodulation in deep-brain regions with widefield, 1,064-nm infrared illumination. Reproduced from [47] with permission from Springer Nature, Copyright 2022.

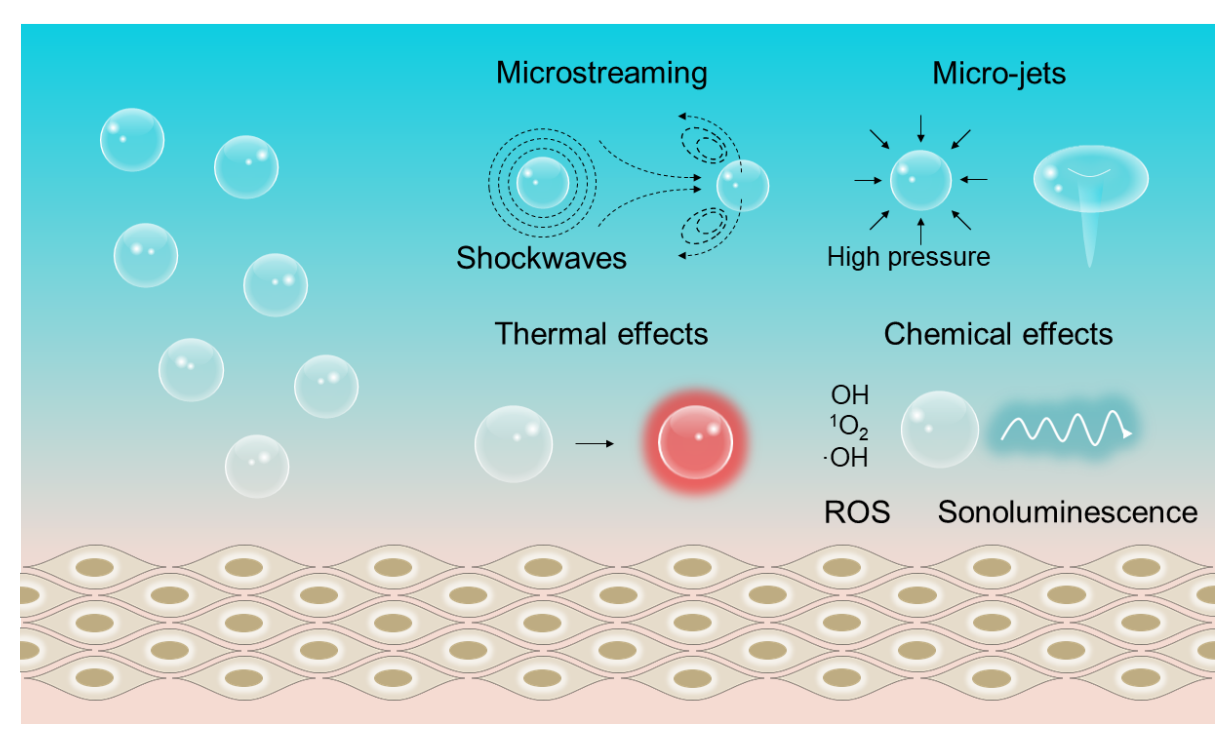


Fig. 2. Interactions of FUS with biological tissues via cavitation. Microstreaming occurs when oscillating bubbles transfer their momentum to the surrounding liquid. At higher pressure amplitudes, microstreaming of the liquid near the bubble can generate shockwaves and micro-jets. Oscillating bubbles can induce acoustic re-radiation and viscous friction to heat their surrounding liquid. The reactive oxygen species and sonoluminescence are produced via the high pressures and temperatures-induced extreme conditions in the core of a collapsing bubble.

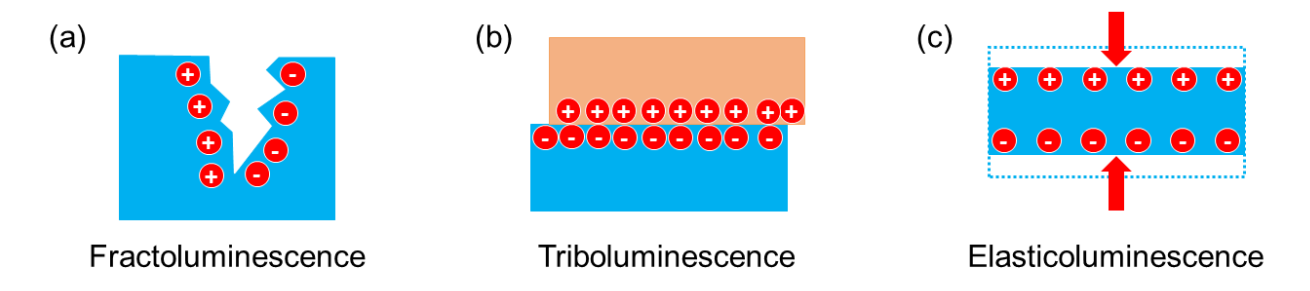


Fig. 3. Schematics of three ML processes. (a) Fractoluminescence; (b) Triboluminescence; (c) Elasticoluminescence.

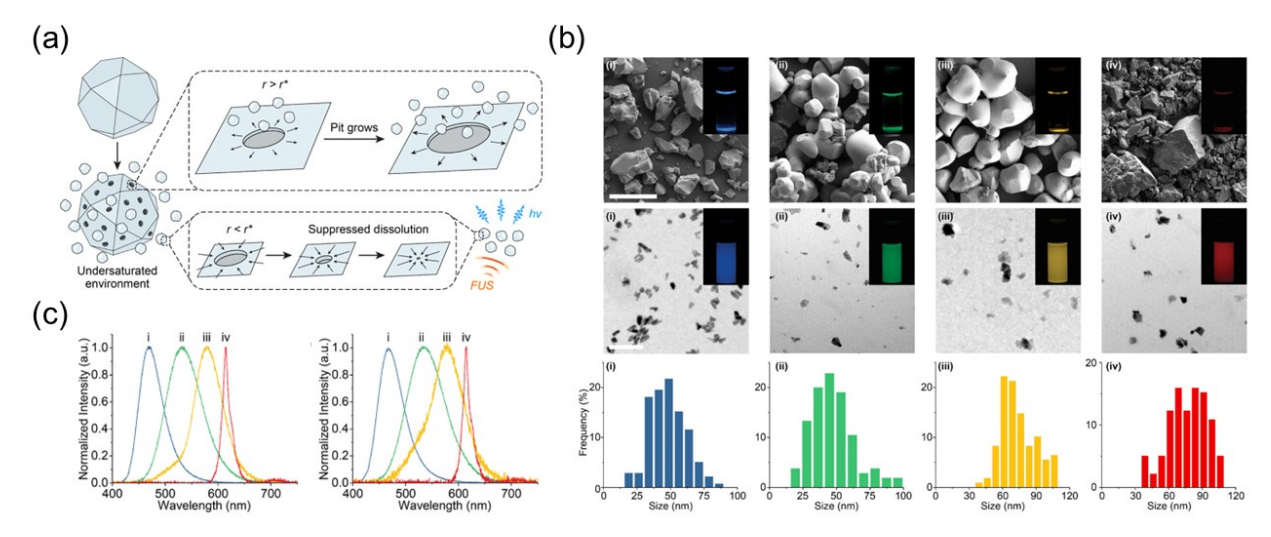


Fig. 4. Preparation of multicolor ML colloidal nanocrystals by a biomineral-inspired method. (a) The biomineral-inspired approach leverages a suppressed dissolution mechanism by learning from natural biominerals to generate ML colloids as a rechargeable internal light source under FUS stimulation. (b) Top: SEM images of (i) Sr₂MgSi₂O₇:Eu,Dy, (ii) ZnS:Cu,Al, (iii) ZnS:Mn, and (iv) CaTiO₃:Pr bulk materials synthesized by solid-state reactions. Scale bars represent 50 μm. Middle: TEM images of (i) Sr₂MgSi₂O₇:Eu,Dy, (ii) ZnS:Cu,Al, (iii) ZnS:Mn, and (iv) CaTiO₃:Pr ML colloidal nanocrystals prepared by the biomineral-inspired approach . Scale bars represent 200 nm. The luminescence images of ML bulk materials and their colloidal nanocrystals in an aqueous solution are inserted in the top and the middle rows. Bottom: size histograms of (i) Sr₂MgSi₂O₇:Eu,Dy, (ii) ZnS:Cu,Al, (iii) ZnS:Mn, and (iv) CaTiO₃:Pr colloidal nanocrystals. (c) Mechanoluminescence spectra of (i) Sr₂MgSi₂O₇:Eu,Dy, (ii) ZnS:Cu,Al, (iii) ZnS:Mn, and (iv) CaTiO₃:Pr bulk materials (left) and their corresponding colloidal nanocrystals (right). Reproduced from [68] with permission from American Chemical Society, Copyright 2022.

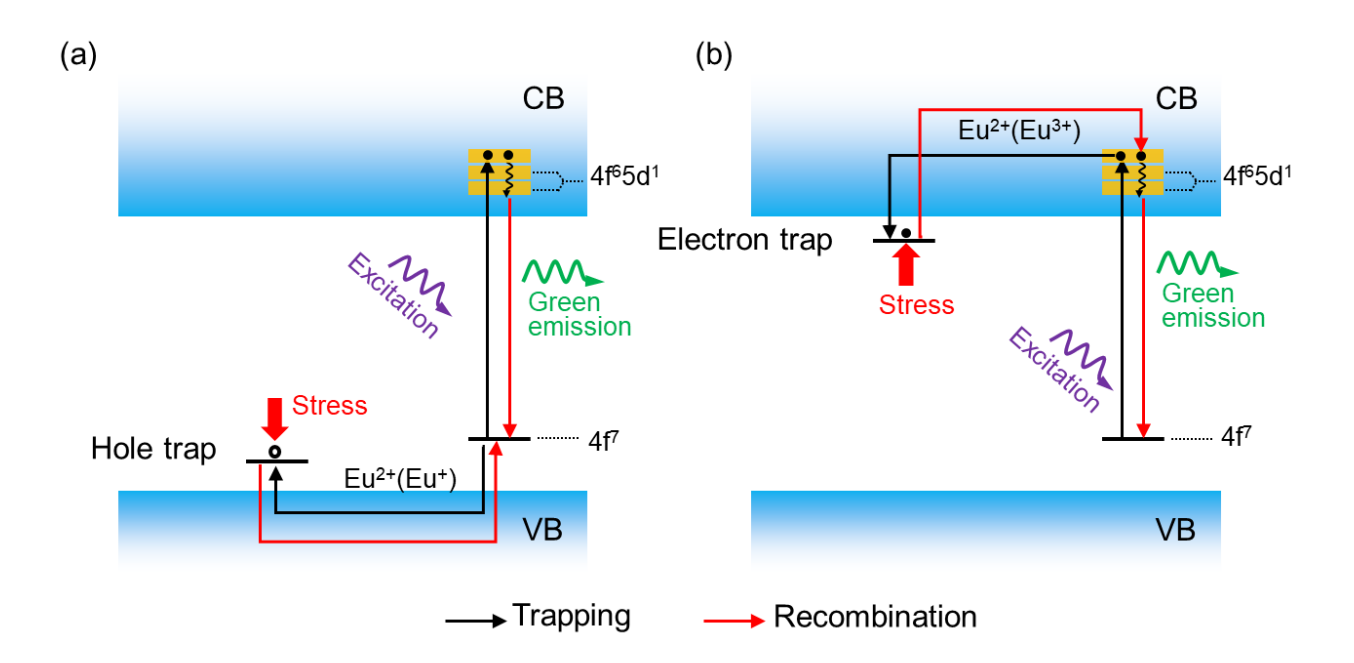


Fig. 5. Schematic diagrams showing the interaction of charge carriers with traps during the ML emission in SrAl₂O₄:Eu²⁺ phosphors. Hole (a) and (b) electron traps serve as the main carrier traps during the ML emission, respectively. VB represents valence band; CB represents conduction band.

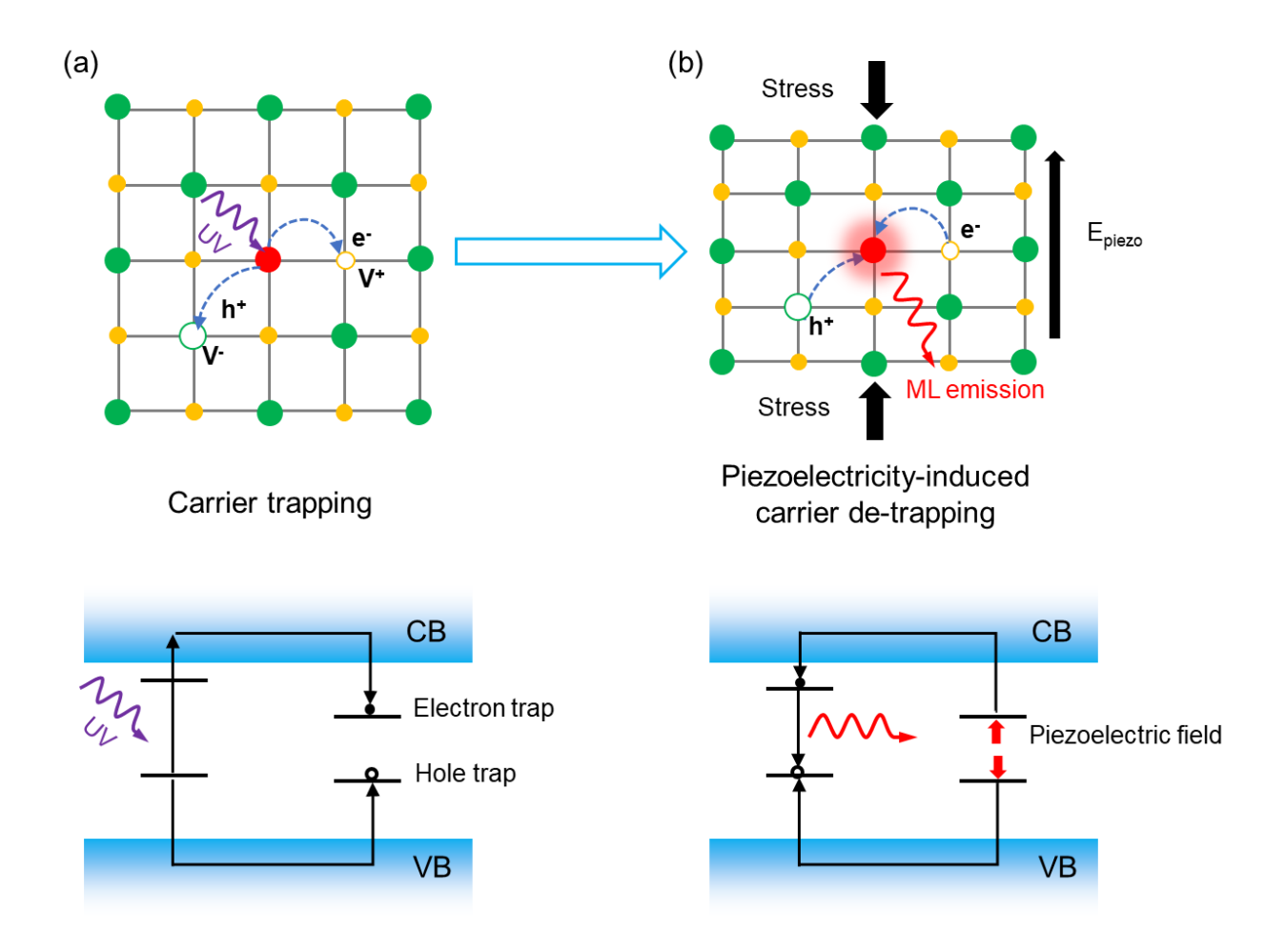


Fig. 6. Schematic of piezoelectricity-induced carrier de-trapping process in the mechanoluminescence process. (a) Carrier trapping in a doped-piezoelectric lattice, (b) Piezoelectricity-induced carrier de-trapping, leading to mechanoluminescence. VB represents valence band; CB represents conduction band.

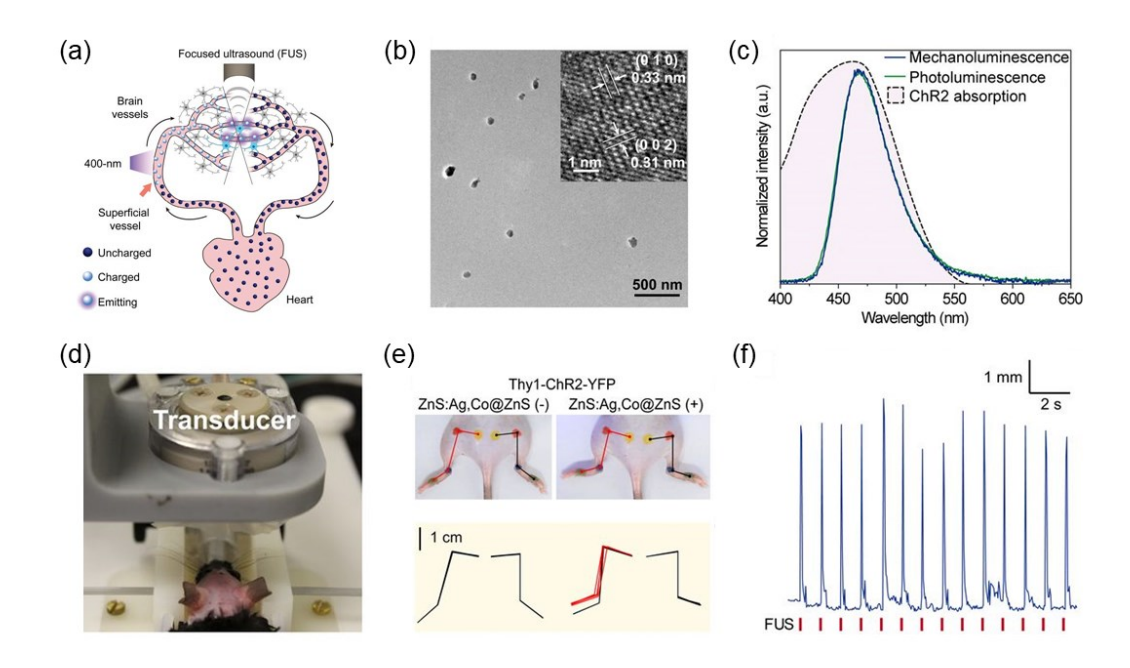


Fig. 7. Sono-optogenetic neuromodulation via FUS-triggered ML emission from MLNTs circulating in the blood. (a) Schematic showing circulation of ZnS:Aq,Co@ZnS MLNTs in blood vessels, which transports 400-nm photoexcited MLNTs at superficial vessels into deep-brain regions to produce 470 nm emission under FUS for optogenetic stimulation. (b) TEM image of ZnS:Ag,Co@ZnS MLNTs and the inset is the highresolution TEM image. (c) Normalized fluorescence (green) and mechanoluminescence (blue) emission spectra of ZnS:Ag,Co@ZnS MLNTs, largely overlapping with the absorption band of ChR2 (the pink shade under black dashed curve). (d) Photograph of sono-optogenetic neuromodulation setup for mouse, highlighting the intact scalp of the shaved mouse. (e) Photographs and hindlimb kinematics of a Thy1-ChR2-YFP mouse during sono-optogenetic neuromodulation through intact scalp, before (Left) and after (Right) injection of ZnS:Aq,Co@ZnS MLNTs. In top images, the kinematics of left and right hindlimbs are shown in red and black lines, respectively. In bottom kinematic diagrams, contralateral limb activation via sono-optogenetic neuromodulation is highlighted in red. (f) Representative hindlimb movement of a Thy1-ChR2-YFP mouse injected with ZnS:Aq,Co@ZnS MLNTs under repetitive FUS stimulation. Reproduced from [23] with permission from National Academy of Sciences, Copyright 2019.

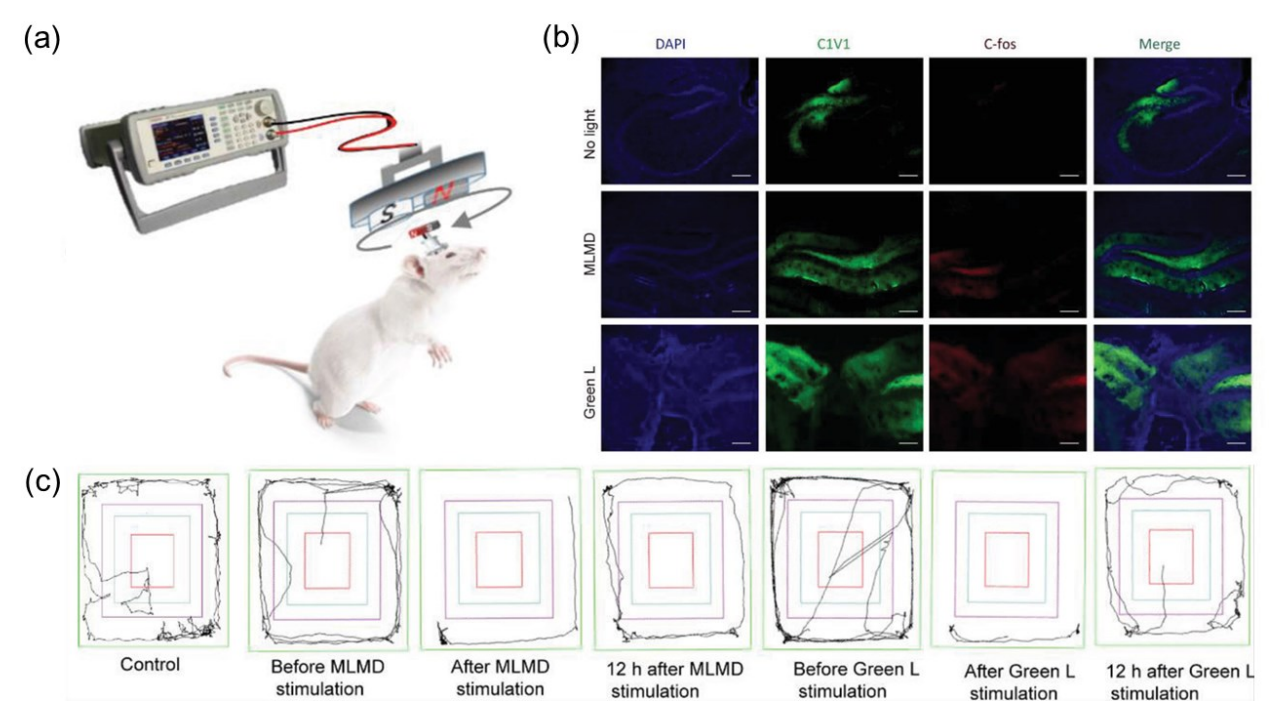


Fig.8. Wireless optogenetics enabled by a MLMD. (a) Schematic showing MLMD device implanted in the primary motor cortex (M1) and the wireless neuromodulation by MLMD in free-moving mice. (b) The confocal images of C1V1 and C-fos staining in hippocampus regions of the mouse brain in different groups. All scale bars represent 200 μm. (c) The displacement trajectories of mice with different neuromodulation conditions. Reproduced from [88] with permission from Wiley-VCH, Copyright 2021.

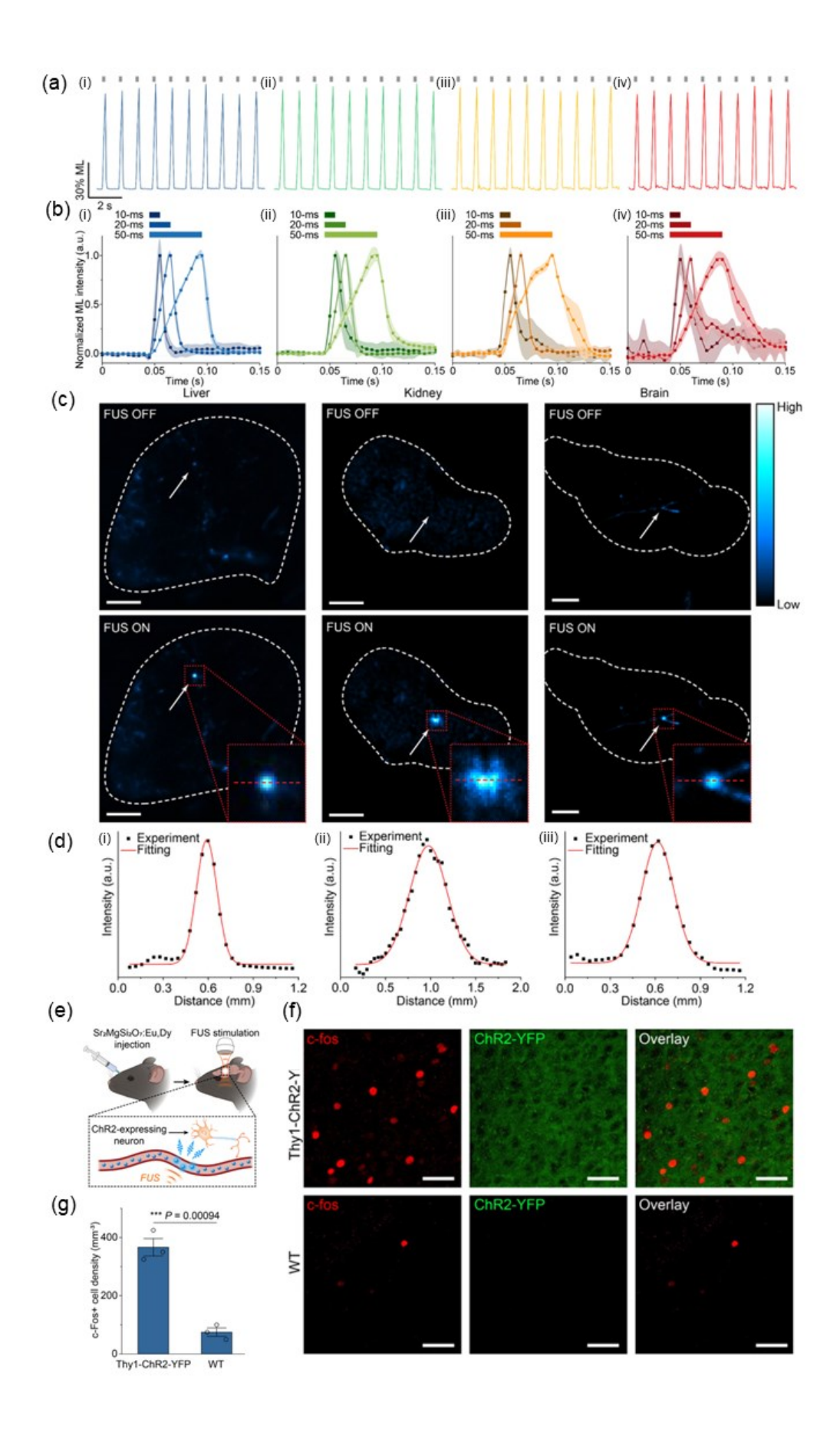


Fig. 9. A biomineralization approach to prepare ML colloidal NPs for sonooptogenetic neural modulation. (a) Rechargeability demonstrated by multicolor ML colloids including: i) Sr₂MgSi₂O₇:Eu,Dy, ii) ZnS:Cu,Al, iii) ZnS:Mn, and iv) CaTiO₃:Pr in an artificial circulation tubing . The FUS pulses were shown as gray ticks above the emission curve. (b) ML temporal kinetics of ML colloids including: i) Sr₂MgSi₂O₇:Eu,Dy, ii) ZnS:Cu,Al, iii) ZnS:Mn, and iv) CaTiO3:Pr upon FUS pulses with different duty cycles in the artificial circulation tubing. (c) Fluorescent images of the mouse organs including: i) liver, ii) kidney, and iii) brain with their blood vessels filled with Sr₂MgSi₂O₇:Eu, Dy ML colloids with FUS off (top) and on (bottom). (d) ML intensity profiles of the emission spots from the mouse organs including: i) liver, ii) kidney, and iii) brain shown as red dashed lines in the inserted figures of (c), respectively. (e) Schematic of in vivo FUS-mediated optogenetic neuromodulation with Sr₂MqSi₂O₇:Eu.Dv colloidal nanocrystals circulation in the motor cortex region of mouse brain. (f) Representative confocal fluorescence images of c-fos staining (left), ChR2-YFP (middle), and the overlay (right) of the same region of the motor cortex in Thy1-ChR2-YFP transgenic (top) and wild-type (bottom) mice after Sr₂MgSi₂O₇:Eu,Dy colloidal nanocrystals were administered, recharged by UV light during blood circulation, and discharged under FUS to produce light emission. All scale bars are 40 µm. (g) Statistical analysis of c-fos+ cells' density for the Thy1-ChR2-YFP and wild-type mice in (f). All data are presented as mean \pm SD. n = 3 mice per group. One-way analysis of variance (ANOVA), *** P < 0.001. Reproduced from [68] with permission from American Chemical Society, Copyright 2022.

References

- [1] S.M. Won, E. Song, J.T. Reeder, J.A. Rogers, Emerging Modalities and Implantable Technologies for Neuromodulation, Cell. 181 (2020) 115–135.
- [2] J.K. Krauss, N. Lipsman, T. Aziz, A. Boutet, P. Brown, J.W. Chang, B. Davidson, W.M. Grill, M.I. Hariz, A. Horn, M. Schulder, A. Mammis, P.A. Tass, J. Volkmann, A.M. Lozano, Technology of deep brain stimulation: current status and future directions, Nat. Rev. Neurol. 17 (2021) 75–87.
- [3] H. Cagnan, T. Denison, C. McIntyre, P. Brown, Emerging technologies for improved deep brain stimulation, Nat. Biotechnol. 37 (2019) 1024–1033.
- [4] P. Verrills, C. Sinclair, A. Barnard, A review of spinal cord stimulation systems for chronic pain, J. Pain Res. 9 (2016) 481–492.
- [5] J. Koo, M.R. MacEwan, S.-K. Kang, S.M. Won, M. Stephen, P. Gamble, Z. Xie, Y. Yan, Y.-Y. Chen, J. Shin, N. Birenbaum, S. Chung, S.B. Kim, J. Khalifeh, D.V. Harburg, K. Bean, M. Paskett, J. Kim, Z.S. Zohny, S.M. Lee, R. Zhang, K. Luo, B. Ji, A. Banks, H.M. Lee, Y. Huang, W.Z. Ray, J.A. Rogers, Wireless bioresorbable electronic system enables sustained nonpharmacological neuroregenerative therapy, Nat. Med. 24 (2018) 1830–1836.
- [6] Y. Zhang, N. Zheng, Y. Cao, F. Wang, P. Wang, Y. Ma, B. Lu, G. Hou, Z. Fang, Z. Liang, M. Yue, Y. Li, Y. Chen, J. Fu, J. Wu, T. Xie, X. Feng, Climbing-inspired twining electrodes using shape memory for peripheral nerve stimulation and recording, Sci Adv. 5 (2019) eaaw1066.
- [7] A.M. Lozano, N. Lipsman, H. Bergman, P. Brown, S. Chabardes, J.W. Chang, K. Matthews, C.C. McIntyre, T.E. Schlaepfer, M. Schulder, Y. Temel, J. Volkmann, J.K. Krauss, Deep brain stimulation: current challenges and future directions, Nat. Rev. Neurol. 15 (2019) 148–160.
- [8] Y. Liu, J. Liu, S. Chen, T. Lei, Y. Kim, S. Niu, H. Wang, X. Wang, A.M. Foudeh, J.B.-H. Tok, Z. Bao, Soft and elastic hydrogel-based microelectronics for localized low-voltage neuromodulation, Nat Biomed Eng. 3 (2019) 58–68.
- [9] F. Zhang, A.M. Aravanis, A. Adamantidis, L. de Lecea, K. Deisseroth, Circuit-breakers: optical technologies for probing neural signals and systems, Nat. Rev. Neurosci. 8 (2007) 577–581.
- [10] K.M. Tye, K. Deisseroth, Optogenetic investigation of neural circuits underlying brain disease in animal models, Nat. Rev. Neurosci. 13 (2012) 251–266.
- [11] K. Deisseroth, P. Hegemann, The form and function of channelrhodopsin, Science. 357 (2017) eaan5544.
- [12] Y. Jiang, J.L. Carvalho-de-Souza, R.C.S. Wong, Z. Luo, D. Isheim, X. Zuo, A.W. Nicholls, I.W. Jung, J. Yue, D.-J. Liu, Y. Wang, V. De Andrade, X. Xiao, L. Navrazhnykh, D.E. Weiss, X. Wu, D.N. Seidman, F. Bezanilla, B. Tian, Heterogeneous silicon mesostructures for lipid-supported bioelectric interfaces, Nat. Mater. 15 (2016) 1023–1030.
- [13] Y. Jiang, X. Li, B. Liu, J. Yi, Y. Fang, F. Shi, X. Gao, E. Sudzilovsky, R. Parameswaran, K. Koehler, V. Nair, J. Yue, K. Guo, Y. Fang, H.-M. Tsai, G. Freyermuth, R.C.S. Wong, C.-M. Kao, C.-T. Chen, A.W. Nicholls, X. Wu, G.M.G. Shepherd, B. Tian, Rational design of silicon structures for optically controlled multiscale biointerfaces, Nat Biomed Eng. 2 (2018) 508–521.

- [14] M. Silverå Ejneby, M. Jakešová, J.J. Ferrero, L. Migliaccio, I. Sahalianov, Z. Zhao, M. Berggren, D. Khodagholy, V. Đerek, J.N. Gelinas, E.D. Głowacki, Chronic electrical stimulation of peripheral nerves via deep-red light transduced by an implanted organic photocapacitor, Nat Biomed Eng. 6 (2022) 741–753.
- [15] G. Hong, A.L. Antaris, H. Dai, Near-infrared fluorophores for biomedical imaging, Nature Biomedical Engineering. 1 (2017) 1–22.
- [16] J.Y. Lin, A user's guide to channelrhodopsin variants: features, limitations and future developments, Exp. Physiol. 96 (2011) 19–25.
- [17] R. Chen, F. Gore, Q.-A. Nguyen, C. Ramakrishnan, S. Patel, S.H. Kim, M. Raffiee, Y.S. Kim, B. Hsueh, E. Krook-Magnusson, I. Soltesz, K. Deisseroth, Deep brain optogenetics without intracranial surgery, Nat. Biotechnol. 39 (2021) 161–164.
- [18] C.N. Bedbrook, K.K. Yang, J.E. Robinson, E.D. Mackey, V. Gradinaru, F.H. Arnold, Machine learning-guided channelrhodopsin engineering enables minimally invasive optogenetics, Nat. Methods. 16 (2019) 1176–1184.
- [19] S. Chen, A.Z. Weitemier, X. Zeng, L. He, X. Wang, Y. Tao, A.J.Y. Huang, Y. Hashimotodani, M. Kano, H. Iwasaki, L.K. Parajuli, S. Okabe, D.B.L. Teh, A.H. All, I. Tsutsui-Kimura, K.F. Tanaka, X. Liu, T.J. McHugh, Near-infrared deep brain stimulation via upconversion nanoparticle-mediated optogenetics, Science. 359 (2018) 679–684.
- [20] R. Prakash, O. Yizhar, B. Grewe, C. Ramakrishnan, N. Wang, I. Goshen, A.M. Packer, D.S. Peterka, R. Yuste, M.J. Schnitzer, K. Deisseroth, Two-photon optogenetic toolbox for fast inhibition, excitation and bistable modulation, Nat. Methods. 9 (2012) 1171–1179.
- [21] W. Yang, R. Yuste, Holographic imaging and photostimulation of neural activity, Curr. Opin. Neurobiol. 50 (2018) 211–221.
- [22] S. Jiang, X. Wu, N.J. Rommelfanger, Z. Ou, G. Hong, Shedding light on neurons: optical approaches for neuromodulation, Natl Sci Rev. 9 (2022) nwac007.
- [23] X. Wu, X. Zhu, P. Chong, J. Liu, L.N. Andre, K.S. Ong, K. Brinson Jr, A.I. Mahdi, J. Li, L.E. Fenno, H. Wang, G. Hong, Sono-optogenetics facilitated by a circulation-delivered rechargeable light source for minimally invasive optogenetics, Proc. Natl. Acad. Sci. U. S. A. 116 (2019) 26332–26342.
- [24] G. Hong, Seeing the sound, Science. 369 (2020) 638.
- [25] R.L. Fork, Laser stimulation of nerve cells in Aplysia, Science. 171 (1971) 907–908.
- [26] A.G. Xu, M. Qian, F. Tian, B. Xu, R.M. Friedman, J. Wang, X. Song, Y. Sun, M.M. Chernov, J.M. Cayce, E.D. Jansen, A. Mahadevan-Jansen, X. Zhang, G. Chen, A.W. Roe, Focal infrared neural stimulation with high-field functional MRI: A rapid way to map mesoscale brain connectomes, Sci Adv. 5 (2019) eaau7046.
- [27] M.G. Shapiro, K. Homma, S. Villarreal, C.-P. Richter, F. Bezanilla, Infrared light excites cells by changing their electrical capacitance, Nat. Commun. 3 (2012) 736.
- [28] M.L. DiFrancesco, F. Lodola, E. Colombo, L. Maragliano, M. Bramini, G.M. Paternò, P. Baldelli, M.D. Serra, L. Lunelli, M. Marchioretto, G. Grasselli, S. Cimò, L. Colella, D. Fazzi, F. Ortica, V. Vurro, C.G. Eleftheriou, D. Shmal, J.F. Maya-Vetencourt, C. Bertarelli, G. Lanzani, F. Benfenati, Neuronal firing modulation by a membrane-targeted photoswitch, Nat. Nanotechnol. 15 (2020) 296–306.
- [29] E.S. Boyden, F. Zhang, E. Bamberg, G. Nagel, K. Deisseroth, Millisecondtimescale, genetically targeted optical control of neural activity, Nat. Neurosci. 8

- (2005) 1263-1268.
- [30] K.L. Montgomery, A.J. Yeh, J.S. Ho, V. Tsao, S. Mohan Iyer, L. Grosenick, E.A. Ferenczi, Y. Tanabe, K. Deisseroth, S.L. Delp, A.S.Y. Poon, Wirelessly powered, fully internal optogenetics for brain, spinal and peripheral circuits in mice, Nat. Methods. 12 (2015) 969–974.
- [31] C. Kathe, F. Michoud, P. Schönle, A. Rowald, N. Brun, J. Ravier, I. Furfaro, V. Paggi, K. Kim, S. Soloukey, L. Asboth, T.H. Hutson, I. Jelescu, A. Philippides, N. Alwahab, J. Gandar, D. Huber, C.I. De Zeeuw, Q. Barraud, Q. Huang, S.P. Lacour, G. Courtine, Wireless closed-loop optogenetics across the entire dorsoventral spinal cord in mice, Nat. Biotechnol. 40 (2022) 198–208.
- [32] R. Qazi, A.M. Gomez, D.C. Castro, Z. Zou, J.Y. Sim, Y. Xiong, J. Abdo, C.Y. Kim, A. Anderson, F. Lohner, S.-H. Byun, B. Chul Lee, K.-I. Jang, J. Xiao, M.R. Bruchas, J.-W. Jeong, Wireless optofluidic brain probes for chronic neuropharmacology and photostimulation, Nat Biomed Eng. 3 (2019) 655–669.
- [33] A.D. Mickle, S.M. Won, K.N. Noh, J. Yoon, K.W. Meacham, Y. Xue, L.A. McIlvried, B.A. Copits, V.K. Samineni, K.E. Crawford, D.H. Kim, P. Srivastava, B.H. Kim, S. Min, Y. Shiuan, Y. Yun, M.A. Payne, J. Zhang, H. Jang, Y. Li, H.H. Lai, Y. Huang, S.-I. Park, R.W. Gereau 4th, J.A. Rogers, A wireless closed-loop system for optogenetic peripheral neuromodulation, Nature. 565 (2019) 361–365.
- [34] A.M. Lozano, N. Lipsman, Probing and regulating dysfunctional circuits using deep brain stimulation, Neuron. 77 (2013) 406–424.
- [35] J.Y. Lin, P.M. Knutsen, A. Muller, D. Kleinfeld, R.Y. Tsien, ReaChR: a red-shifted variant of channelrhodopsin enables deep transcranial optogenetic excitation, Nat. Neurosci. 16 (2013) 1499–1508.
- [36] A.M. Aravanis, L.-P. Wang, F. Zhang, L.A. Meltzer, M.Z. Mogri, M.B. Schneider, K. Deisseroth, An optical neural interface: in vivo control of rodent motor cortex with integrated fiberoptic and optogenetic technology, J. Neural Eng. 4 (2007) S143–56.
- [37] F. Pisanello, G. Mandelbaum, M. Pisanello, I.A. Oldenburg, L. Sileo, J.E. Markowitz, R.E. Peterson, A. Della Patria, T.M. Haynes, M.S. Emara, B. Spagnolo, S.R. Datta, M. De Vittorio, B.L. Sabatini, Dynamic illumination of spatially restricted or large brain volumes via a single tapered optical fiber, Nat. Neurosci. 20 (2017) 1180–1188.
- [38] H. Acarón Ledesma, X. Li, J.L. Carvalho-de-Souza, W. Wei, F. Bezanilla, B. Tian, An atlas of nano-enabled neural interfaces, Nat. Nanotechnol. 14 (2019) 645–657.
- [39] J.W. Salatino, K.A. Ludwig, T.D.Y. Kozai, E.K. Purcell, Glial responses to implanted electrodes in the brain, Nat Biomed Eng. 1 (2017) 862–877.
- [40] C.T. Wentz, J.G. Bernstein, P. Monahan, A. Guerra, A. Rodriguez, E.S. Boyden, A wirelessly powered and controlled device for optical neural control of freelybehaving animals, J. Neural Eng. 8 (2011) 046021.
- [41] J.H. Marshel, Y.S. Kim, T.A. Machado, S. Quirin, B. Benson, J. Kadmon, C. Raja, A. Chibukhchyan, C. Ramakrishnan, M. Inoue, J.C. Shane, D.J. McKnight, S. Yoshizawa, H.E. Kato, S. Ganguli, K. Deisseroth, Cortical layer-specific critical dynamics triggering perception, Science. 365 (2019) eaaw5202.
- [42] A.S. Chuong, M.L. Miri, V. Busskamp, G.A.C. Matthews, L.C. Acker, A.T. Sørensen, A. Young, N.C. Klapoetke, M.A. Henninger, S.B. Kodandaramaiah, M. Ogawa, S.B. Ramanlal, R.C. Bandler, B.D. Allen, C.R. Forest, B.Y. Chow, X. Han,

- Y. Lin, K.M. Tye, B. Roska, J.A. Cardin, E.S. Boyden, Noninvasive optical inhibition with a red-shifted microbial rhodopsin, Nat. Neurosci. 17 (2014) 1123–1129.
- [43] X. Gong, D. Mendoza-Halliday, J.T. Ting, T. Kaiser, X. Sun, A.M. Bastos, R.D. Wimmer, B. Guo, Q. Chen, Y. Zhou, M. Pruner, C.W.-H. Wu, D. Park, K. Deisseroth, B. Barak, E.S. Boyden, E.K. Miller, M.M. Halassa, Z. Fu, G. Bi, R. Desimone, G. Feng, An Ultra-Sensitive Step-Function Opsin for Minimally Invasive Optogenetic Stimulation in Mice and Macaques, Neuron. 107 (2020) 38–51.e8.
- [44] T. Miyazaki, S. Chowdhury, T. Yamashita, T. Matsubara, H. Yawo, H. Yuasa, A. Yamanaka, Large Timescale Interrogation of Neuronal Function by Fiberless Optogenetics Using Lanthanide Micro-particles, Cell Rep. 26 (2019) 1033–1043.e5.
- [45] X. Liu, H. Chen, Y. Wang, Y. Si, H. Zhang, X. Li, Z. Zhang, B. Yan, S. Jiang, F. Wang, S. Weng, W. Xu, D. Zhao, J. Zhang, F. Zhang, Near-infrared manipulation of multiple neuronal populations via trichromatic upconversion, Nat. Commun. 12 (2021) 5662.
- [46] E.O. Gracheva, N.T. Ingolia, Y.M. Kelly, J.F. Cordero-Morales, G. Hollopeter, A.T. Chesler, E.E. Sánchez, J.C. Perez, J.S. Weissman, D. Julius, Molecular basis of infrared detection by snakes, Nature. 464 (2010) 1006–1011.
- [47] X. Wu, Y. Jiang, N.J. Rommelfanger, F. Yang, Q. Zhou, R. Yin, J. Liu, S. Cai, W. Ren, A. Shin, K.S. Ong, K. Pu, G. Hong, Tether-free photothermal deep-brain stimulation in freely behaving mice via wide-field illumination in the near-infrared-II window, Nat Biomed Eng. 6 (2022) 754–770.
- [48] A.S. Kalmbach, J. Waters, Brain surface temperature under a craniotomy, J. Neurophysiol. 108 (2012) 3138–3146.
- [49] M. Manzano, M. Vallet-Regí, Ultrasound responsive mesoporous silica nanoparticles for biomedical applications, Chem. Commun. 55 (2019) 2731–2740.
- [50] E. Stride, C. Coussios, Nucleation, mapping and control of cavitation for drug delivery, Nat. Rev. Phys. 1 (2019) 495–509.
- [51] N. Vyas, K. Manmi, Q. Wang, A.J. Jadhav, M. Barigou, R.L. Sammons, S.A. Kuehne, A.D. Walmsley, Which Parameters Affect Biofilm Removal with Acoustic Cavitation? A Review, Ultrasound Med. Biol. 45 (2019) 1044–1055.
- [52] J. Jalal, T.S.H. Leong, Microstreaming and Its Role in Applications: A Mini-Review, Fluids. 3 (2018) 93.
- [53] L. Tu, Z. Liao, Z. Luo, Y. Wu, A. Herrmann, S. Huo, Ultrasound-controlled drug release and drug activation for cancer therapy, Exploration. 1 (2021) 20210023.
- [54] M. Enayati, D. al Mohazey, M. Edirisinghe, E. Stride, Ultrasound-stimulated drug release from polymer micro and nanoparticles, Bioinspired Biomim. Nanobiomaterials. 2 (2013) 3–10.
- [55] A. Schroeder, J. Kost, Y. Barenholz, Ultrasound, liposomes, and drug delivery: principles for using ultrasound to control the release of drugs from liposomes, Chem. Phys. Lipids. 162 (2009) 1–16.
- [56] Z. Izadifar, Z. Izadifar, D. Chapman, P. Babyn, An Introduction to High Intensity Focused Ultrasound: Systematic Review on Principles, Devices, and Clinical Applications, J. Clin. Med. Res. 9 (2020) 460.
- [57] W. Wang, A. Tasset, I. Pyatnitskiy, H.G. Mohamed, R. Taniguchi, R. Zhou, M. Rana, P. Lin, S.L.C. Capocyan, A. Bellamkonda, W. Chase Sanders, H. Wang, Ultrasound triggered organic mechanoluminescence materials, Adv. Drug Deliv.

- Rev. 186 (2022) 114343.
- [58] F. Bacon, The Advancement of Learning [1605], in: Primer of Intellectual Freedom, Harvard University Press, 2013: pp. 172–192.
- [59] J.I. Zink, G.E. Hardy, J.E. Sutton, Triboluminescence of sugars, J. Phys. Chem. 80 (1976) 248–249.
- [60] R. Boyle, Experiments and Considerations Touching Colours: First Occasionally Written, Among Some Other Essays, to a Friend; and Now Suffer'd to Come Abroad as the Beginning of an Experimental History of Colours, 1664.
- [61] C.-N. Xu, T. Watanabe, M. Akiyama, X.-G. Zheng, Direct view of stress distribution in solid by mechanoluminescence, Appl. Phys. Lett. 74 (1999) 2414–2416.
- [62] C.N. Xu, T. Watanabe, M. Akiyama, X.G. Zheng, Artificial skin to sense mechanical stress by visible light emission, Appl. Phys. Lett. 74 (1999) 1236–1238.
- [63] N. Terasaki, C.-N. Xu, C. Li, L. Zhang, C. Li, D. Ono, M. Tsubai, Y. Adachi, Y. Imai, N. Ueno, T. Shinokawa, Visualization of active crack on bridge in use by mechanoluminescent sensor, in: K. Tribikram (Ed.), Health Monitoring of Structural and Biological Systems 2012, 2012: p. 83482D.
- [64] L. Liu, C.N. Xu, A. Yoshida, D. Tu, N. Ueno, S. Kainuma, Scalable Elasticoluminescent Strain Sensor for Precise Dynamic Stress Imaging and Onsite Infrastructure Diagnosis, Adv. Mater. Technol. 4 (2019) 1800336.
- [65] Y. Zhang, Y. Fang, J. Li, Q. Zhou, Y. Xiao, K. Zhang, B. Luo, J. Zhou, B. Hu, Dual-Mode Electronic Skin with Integrated Tactile Sensing and Visualized Injury Warning, ACS Appl. Mater. Interfaces. 9 (2017) 37493–37500.
- [66] K. Hyodo, Y. Terasawa, C.-N. Xu, H. Sugaya, H. Mishima, S. Miyakawa, MECHANOLUMINESCENT STRESS IMAGING FOR HARD TISSUE BIOMECHANICS, J. Biomech. 45 (2012) S263.
- [67] D. Hardman, T. George Thuruthel, F. Iida, Self-healing ionic gelatin/glycerol hydrogels for strain sensing applications, NPG Asia Materials. 14 (2022) 11.
- [68] F. Yang, X. Wu, H. Cui, S. Jiang, Z. Ou, S. Cai, G. Hong, Palette of Rechargeable Mechanoluminescent Fluids Produced by a Biomineral-Inspired Suppressed Dissolution Approach, J. Am. Chem. Soc. 144 (2022) 18406–18418.
- [69] X.Y. Wei, X. Wang, S.Y. Kuang, L. Su, H.Y. Li, Y. Wang, C. Pan, Z.L. Wang, G. Zhu, Dynamic Triboelectrification-Induced Electroluminescence and its Use in Visualized Sensing, Adv. Mater. 28 (2016) 6656–6664.
- [70] B.P. Chandra, Mechanoluminescence induced by elastic deformation of coloured alkali halide crystals using pressure steps, J. Lumin. 128 (2008) 1217–1224.
- [71] N. Brahme, M. Shukla, D.P. Bisen, U. Kurrey, A. Choubey, R.S. Kher, M. Singh, Mechanoluminescence by impulsive deformation of γ-irradiated Er-doped CaF2 crystals, J. Lumin. 131 (2011) 965–969.
- [72] A. Tiwari, S.A. Khan, R.S. Kher, M. Mehta, S.J. Dhoble, Effect of capping on the mechanoluminescence of γ-irradiated ZnS:Cu nanophosphors, J. Lumin. 131 (2011) 1172–1176.
- [73] J.-C. Zhang, X. Wang, G. Marriott, C.-N. Xu, Trap-controlled mechanoluminescent materials, Prog. Mater Sci. 103 (2019) 678–742.
- [74] S. Gai, C. Li, P. Yang, J. Lin, Recent progress in rare earth micro/nanocrystals: soft chemical synthesis, luminescent properties, and biomedical applications, Chem. Rev. 114 (2014) 2343–2389.

- [75] S. Rahemi Ardekani, A. Sabour Rouh Aghdam, M. Nazari, A. Bayat, E. Yazdani, E. Saievar-Iranizad, A comprehensive review on ultrasonic spray pyrolysis technique: Mechanism, main parameters and applications in condensed matter, J. Anal. Appl. Pyrolysis. 141 (2019) 104631.
- [76] P. Majerič, R. Rudolf, Advances in Ultrasonic Spray Pyrolysis Processing of Noble Metal Nanoparticles—Review, Materials. 13 (2020) 3485.
- [77] C. Li, Y. Imai, Y. Adachi, H. Yamada, K. Nishikubo, C.-N. Xu, One-Step Synthesis of Luminescent Nanoparticles of Complex Oxide, Strontium Aluminate, J. Am. Ceram. Soc. 90 (2007) 2273–2275.
- [78] F. Yang, X. Wu, H. Cui, Z. Ou, S. Jiang, S. Cai, Q. Zhou, B.G. Wong, H. Huang, G. Hong, A biomineral-inspired approach of synthesizing colloidal persistent phosphors as a multicolor, intravital light source, Sci Adv. 8 (2022) eabo6743.
- [79] H. Yamada, X. Fu, C.-N. Xu, Enhancement of Adhesion and Triboluminescent Properties of SrAl2O4: Eu2 + Films Fabricated by RF Magnetron Sputtering and Postannealing Techniques, J. Electrochem. Soc. 154 (2007) J348.
- [80] C.-N. Xu, H. Yamada, X. Wang, X.-G. Zheng, Strong elasticoluminescence from monoclinic-structure SrAl2O4, Appl. Phys. Lett. 84 (2004) 3040–3042.
- [81] J.-C. Zhang, X. Wang, X. Yao, C.-N. Xu, H. Yamada, Strong Elastico-Mechanoluminescence in Diphase (Ba, Ca) TiO3: Pr3 + with Self-Assembled Sandwich Architectures, J. Electrochem. Soc. 157 (2010) G269.
- [82] H. Zhang, H. Yamada, N. Terasaki, C.-N. Xu, Green Mechanoluminescence of Ca2MgSi2O7: Eu and Ca2MgSi2O7: Eu,Dy, J. Electrochem. Soc. 155 (2007) J55.
- [83] L. Zhang, C.-N. Xu, H. Yamada, N. Bu, Enhancement of Mechanoluminescence in CaAl2Si2O8: Eu2 + by Partial Sr2 + Substitution for Ca2 +, J. Electrochem. Soc. 157 (2010) J50.
- [84] H. Zhang, N. Terasaki, H. Yamada, C.-N. Xu, Mechanoluminescence of Europium-Doped SrAMgSi2O7 (A=Ca, Sr, Ba), Jpn. J. Appl. Phys. 48 (2009) 04C109.
- [85] X. Wang, H. Zhang, R. Yu, L. Dong, D. Peng, A. Zhang, Y. Zhang, H. Liu, C. Pan, Z.L. Wang, Dynamic pressure mapping of personalized handwriting by a flexible sensor matrix based on the mechanoluminescence process, Adv. Mater. 27 (2015) 2324–2331.
- [86] X. Wang, M. Que, M. Chen, X. Han, X. Li, C. Pan, Z.L. Wang, Full Dynamic-Range Pressure Sensor Matrix Based on Optical and Electrical Dual-Mode Sensing, Adv. Mater. 29 (2017) 1605817.
- [87] X.Y. Wei, L. Liu, H.L. Wang, S.Y. Kuang, X. Zhu, Z.L. Wang, Y. Zhang, G. Zhu, High-Intensity Triboelectrification-Induced Electroluminescence by Microsized Contacts for Self-Powered Display and Illumination, Adv. Mater. Interfaces. 5 (2018) 1701063.
- [88] Y. Zhang, X. Zhang, H. Wang, Y. Tian, H. Pan, L. Zhang, F. Wang, J. Chang, Remote Regulation of Optogenetic Proteins by a Magneto-Luminescence Microdevice, Adv. Funct. Mater. 31 (2021) 2006357.
- [89] J.-W. Yoo, E. Chambers, S. Mitragotri, Factors that control the circulation time of nanoparticles in blood: challenges, solutions and future prospects, Curr. Pharm. Des. 16 (2010) 2298–2307.
- [90] C. Jia, Y. Xia, Y. Zhu, M. Wu, S. Zhu, X. Wang, High-Brightness, High-Resolution, and Flexible Triboelectrification-Induced Electroluminescence Skin for Real-Time

- Imaging and Human–Machine Information Interaction, Adv. Funct. Mater. 32 (2022) 2201292.
- [91] Y. Xie, Z. Li, The development of mechanoluminescence from organic compounds: breakthrough and deep insight, Mater. Chem. Front. 4 (2020) 317–331.
- [92] Y. Zhang, Z. Wang, T.B. Kouznetsova, Y. Sha, E. Xu, L. Shannahan, M. Fermen-Coker, Y. Lin, C. Tang, S.L. Craig, Distal conformational locks on ferrocene mechanophores guide reaction pathways for increased mechanochemical reactivity, Nat. Chem. 13 (2021) 56–62.
- [93] C. Zhang, J. Huang, Z. Zeng, S. He, P. Cheng, J. Li, K. Pu, Catalytical nano-immunocomplexes for remote-controlled sono-metabolic checkpoint trimodal cancer therapy, Nat. Commun. 13 (2022) 3468.
- [94] Z. Zeng, C. Zhang, S. He, J. Li, K. Pu, Activatable Cancer Sono-Immunotherapy using Semiconducting Polymer Nanobodies, Adv. Mater. 34 (2022) e2203246.
- [95] W. Wang, X. Wu, K.W. Kevin Tang, I. Pyatnitskiy, R. Taniguchi, P. Lin, R. Zhou, S.L.C. Capocyan, G. Hong, H. Wang, Ultrasound-Triggered In Situ Photon Emission for Noninvasive Optogenetics, J. Am. Chem. Soc. (2023). https://doi.org/10.1021/jacs.2c10666.
- [96] R.L. Auten, J.M. Davis, Oxygen toxicity and reactive oxygen species: the devil is in the details, Pediatr. Res. 66 (2009) 121–127.
- [97] C. Lehner, R. Gehwolf, H. Tempfer, I. Krizbai, B. Hennig, H.-C. Bauer, H. Bauer, Oxidative stress and blood-brain barrier dysfunction under particular consideration of matrix metalloproteinases, Antioxid. Redox Signal. 15 (2011) 1305–1323.
- [98] M.L. Prieto, O. Ömer, B.T. Khuri-Yakub, M.C. Maduke, Dynamic response of model lipid membranes to ultrasonic radiation force, PLoS One. 8 (2013) e77115.
- [99] S. Yoo, D.R. Mittelstein, R.C. Hurt, J. Lacroix, M.G. Shapiro, Focused ultrasound excites cortical neurons via mechanosensitive calcium accumulation and ion channel amplification, Nat. Commun. 13 (2022) 493.
- [100] H.A.S. Kamimura, A. Conti, N. Toschi, E.E. Konofagou, Ultrasound neuromodulation: mechanisms and the potential of multimodal stimulation for neuronal function assessment, Front. Phys. 8 (2020) 150.
- [101] T. Sato, M.G. Shapiro, D.Y. Tsao, Ultrasonic Neuromodulation Causes Widespread Cortical Activation via an Indirect Auditory Mechanism, Neuron. 98 (2018) 1031–1041.e5.
- [102] H. Guo, M. Hamilton 2nd, S.J. Offutt, C.D. Gloeckner, T. Li, Y. Kim, W. Legon, J.K. Alford, H.H. Lim, Ultrasound Produces Extensive Brain Activation via a Cochlear Pathway, Neuron. 98 (2018) 1020–1030.e4.
- [103] P.P. Ye, J.R. Brown, K.B. Pauly, Frequency Dependence of Ultrasound Neurostimulation in the Mouse Brain, Ultrasound Med. Biol. 42 (2016) 1512–1530.
- [104] K. Yu, X. Niu, E. Krook-Magnuson, B. He, Intrinsic functional neuron-type selectivity of transcranial focused ultrasound neuromodulation, Nat. Commun. 12 (2021) 2519.
- [105] F. Yang, H. Cui, X. Wu, S.-J. Kim, G. Hong, Ultrasound-activated luminescence with color tunability enabled by mechanoluminescent colloids and perovskite quantum dots, Nanoscale. (2023). https://doi.org/10.1039/D2NR06129E.